



Norwegian University of
Science and Technology

Simulating Sun Vector Estimation and Finding Gyroscopes for the NUTS Project

Henrik Rudi Haave

Master of Science in Cybernetics and Robotics

Submission date: June 2016

Supervisor: Jan Tommy Gravdahl, ITK

Norwegian University of Science and Technology
Department of Engineering Cybernetics

Simulating Sun Vector Estimation and Finding Gyroscopes for the NUTS Project

Henrik Rudi Haave

Jun 2016

MASTER THESIS

Department of Engineering Cybernetics
Norwegian University of Science and Technology

Supervisor 1: Jan Tommy Gravdahl, ITK

Preface

This Masters thesis is a contribution to the attitude estimation and control system for the NTNU test satellite project. The work was carried out on the Spring semester of 2016 and is not a direct continuation of the Project thesis. This work is focused on two of the sensors needed for the attitude determination and control system. Namely the Sun Sensor and the Gyroscope. A large part of the work done here stands on Antione Pigneds work on the satellite prediction algorithms done during the spring semester 2015

Trondheim, 2016-06-29

Henrik Rudi Haave

Acknowledgment

I would like to acknowledge the help and support from family and friends during difficult times of this work. Without them this work may not have been completed in any fashion at all. Secondly my supervisor Jan Tommy Grasdahl must be thanked for his patience and willingness to participate on this thesis. Lastly Roger Birkeland and Amund Gjersvik leading the NUTS project is thanked for their time help and support provided.

H.R.H

Summary and Conclusions

The attitude estimation and control system is completely dependent on sensor input to perform its task of finding the satellites orientation and rotation rate. The three types of sensors are needed to complete such a task with sufficient accuracy to point the satellite. A Gyroscope for measurement of rotation rate. A Sun sensor for measurement of the first reference vector, and a Magnetometer providing the last reference vector needed for a full orientation estimate. Large uncertainties were present in regards to the accuracy of the Sun sensor prototype consisting of 6 photodiodes mounted on each side of the satellite. The accuracy problem stems from the known fact that reflected light from Earth often gives large errors on the measured Sun vector. Also this prototype of the Sun sensor has no redundancy a problem that absolutely needed to be alleviated. Because of this the following work has been done on the Sun sensor.

- **Simulation** of Sun and Earth irradiance incident on a satellite in Earth orbit
- **A improvement** to the Sun sensor prototype has been suggested and simulated with Sun irradiance and Earth irradiance as the only error source. It is shown that the new configuration of photodiodes allows for both redundancy and limiting of field of view(FOV). Alternative photodiodes have been reviewed and two new photodiodes has been suggested and are expected to improve measurements significantly.
- **Two new Sun vector estimation** algorithms have been suggested for the new configuration of photodiodes. They use the FOV limits physically applied to the photodiodes and the redundant design, improving mean error peaks to almost below 5[deg] for the majority of Sun lit orbit time.

It was discovered in past work that the attitude controller was very sensitive to error in the rotation rate. Significant work was therefor completed with regards to the choice of a new gyroscope.

- **Microelectromechanical** systems(MEMS) Gyroscope possible Error sources and models were thoroughly investigated and it was found that datasheets were wholly unreliable for choosing a final gyroscope to the NUTS Cube Satellite. Literature clearly indicates that temperature dependent bias on gyroscopes may have different properties depending on the gyroscope.
- **Three Gyroscopes** are suggested for further investigation to find out if they are sufficiently good to make the attitude controller work. These gyroscopes were chosen from a larger set put together from all relevant manufacturers of gyroscopes found. A single gyroscope could not be decided upon partially because finding an off-the-shelf gyroscope with both good noise characteristics and bias stability with respect to temperature variations was discovered to be difficult.

Contents

Preface	i
Acknowledgment	ii
Summary and Conclusions	iii
1 Introduction	2
1.1 Background	2
1.2 Objectives	3
1.3 Structure of the Report	4
2 Background Material	5
2.1 Coordinate Systems	5
2.1.1 Earth Centered Inertial Frame	5
2.1.2 Earth Centered Earth Fixed Frame	6
2.1.3 Body Frame	6
2.2 Temperature Variations	7
2.2.1 Thermal analysis	7
2.2.2 Post flight report	7
2.3 Satellite Irradiance	9
2.3.1 Radiance, Irradiance, and Reflected light	9
2.3.2 Sun Irradiance	12
2.3.3 Earth Irradiance	14
2.3.4 Earth Reflection Model	20
2.4 Sun Sensors	22

2.4.1	PIN Photodiodes	22
2.4.2	Position Sensitive Diode(PSD)	29
2.4.3	Quadrant Photodiodes	31
2.5	MEMS Gyroscope Errors	32
2.5.1	Scale Factor(δS_G)	34
2.5.2	Misalignment Error (M_G)	35
2.5.3	Bias(B_g)	35
2.5.4	Thermo Mechanical White Noise(ϵ_G)	38
3	Choosing Sensors	39
3.1	Finding And Evaluating Gyroscope Alternatives	39
3.1.1	Reading data sheets	39
3.1.2	Evaluating Alternatives	42
3.2	Sun Sensor Design	46
3.2.1	Sun Sensor Choice	46
3.2.2	Photocurrent Equations	46
3.2.3	Choosing A PIN Photodiode	48
3.2.4	Mounting Orientation	53
4	Simulation of Sun Sensor output and Sun Vector Estimation	57
4.1	Environmental Input Model	58
4.1.1	ECI,ECEF Frame Rotation	59
4.1.2	SGP4 Orbit Model	60
4.1.3	Sun Vector Model	60
4.1.4	Earth Shadowing	61
4.1.5	Albedo Model	63
4.2	Satellite Sensor Hardware	65
4.2.1	Photodiode Output	65
4.2.2	Operational Amplifier and ADC	67
4.3	Sun Vector Estimation	70
4.3.1	Pseudoinverse	71

<i>CONTENTS</i>	1
4.3.2 Linear Least Squares Sun Vector Estimation	74
4.3.3 Albedo-Sun Vector Estimate	77
4.3.4 Sun-Albedo-Sun Vector Estimate	81
5 Summary	85
5.1 Summary and Conclusion	85
5.2 Discussion	87
5.3 Further Work	88
Bibliography	90

Chapter 1

Introduction

The work presented in this master thesis is for the attitude determination and control system on The Norwegian University Of Science and Technology (NTNU) test satellite (NUTS). More specifically this is a pico satellite following the standard of Cube Satellites with dimensions $10 \times 10 \times 20$ [mm], often termed as a double Cube satellite. The project was launched in 2010 and is currently under development with a camera as payload and an experimental carbon frame instead of the standard frame of aluminium. This student satellite program is one of three driven by the Norwegian Center for Space-related Education (NAROM).

1.1 Background

At this point in the NUTS Cube Sat program it is seen that previous work done by Øyvind Rein [Øyvind Rein \(2014\)](#) on the attitude determination and control system (ADCS) had significant room for improvement with regards to the sensor choice. Several of the sensors chosen were not reasoned for and there is no knowledge in the project on the accuracy achievable with the

Sun sensor solution. Also very little work was done to find good Sun Vector estimation algorithms for the sensor. It is therefore chosen as a goal here to properly reason for and suggest a Sun sensor solution. Testing a Sun sensor solution for the case of a Earth orbiting satellite is not really viable here on Earth surface in an efficient way. It therefore seems natural to implement a simulation of Sun and Earth reflected irradiance incident on a satellite in Earth orbit as a tool for verifying the suggested solutions.

Marius Westgard [Westgård \(2015\)](#) found in his masters thesis that very small amounts of rotation rate error lead to failure of satellite pointing algorithm. An attempt will therefore be made here to find a sufficiently good gyroscope for the nuts Cube Sat. But this author is very unfamiliar with gyroscopes in general. Therefore knowledge on gyroscope error models seems like the first objective that needs to be completed before the market of gyroscopes can be searched for an alternative. Concrete objectives are given below for Sun sensor goals and the gyroscope goals

1.2 Objectives

- Find and present significant knowledge on Microelectromechanical systems (MEMS) Gyroscope error models for sufficient background to support a choice of gyroscope using datasheets.
- Compile an overview of the most relevant gyroscopes available for use on the NUTS project and make a recommendation based on the knowledge attained.
- Simulate Sun and Earth reflected irradiance incident on a satellite orbiting Earth.
- Suggest a Sun sensor solution with priority on robustness and redundancy that can provide measurements needed to estimate a Sun vector of accuracy better than $5[deg]$ and simulate sensor measurement
- Suggest a Sun vector estimation algorithm that provides the estimated Sun vector of accuracy better than $5[deg]$

1.3 Structure of the Report

Chapter 2 This chapter covers all of the background material used to complete the objectives stated in this chapter. This means that the first objective for the Gyroscope is answered here. There is also information present that is not directly used but still relevant.

Chapter 3 Here the found gyroscopes on the market are presented and a recommendation is given before a Sun sensor is suggested and reasoned for.

Chapter 4 First the implementation of simulated irradiance from the Sun and Earth is described. Then the implementation of the simulated Sun sensor suggested in Chapter 3 is given. Before the Sun vector estimation algorithms are suggested, described and simulated.

Chapter 5 Summary and conclusions

Chapter 2

Background Material

2.1 Coordinate Systems

In complex systems with several moving objects and related physical values that one wishes to observe from a moving body. Several coordinate systems is needed to represent the relation between these values. These coordinate systems are implemented as frames of reference used in this thesis and described bellow. Notation used for vectors and rotation matrices is taken from "Handbook of Marine Craft Hydrodynamics and Motion Control" [Fossen \(2011\)](#)

2.1.1 Earth Centered Inertial Frame

All motion must be described with respect to a inert(non accelerating) reference frame. Because Earth rotates around the Sun, and itself while the Sun rotates around the milky-way, fixing a frame to either of them dose not give a true inert frame. But for most practical purposes a Earth

Centered Inertial(ECI) frame is used. Roughly speaking most ECI Coordinate Systems are defined with the x axis pointing in the direction of the Northern/Vernal(spring) equinox and the z axis pointing along Earth's rotational axis. There are many ECI systems with differing precision because Earth's rotational axis changes with time. One such system is the celestial reference system(CRS) defined with its origin at Earth's center of mass, the x direction as the mean Vernal equinox vector at J2000.0 epoch, and the z axis perpendicular to mean equator at J2000.0 epoch pointing northward. A implementation of a CRS goes under the name (conventional)Celestial Reference Frame(CRF).

2.1.2 Earth Centered Earth Fixed Frame

A ECEF frame or if one wants the conventional Terrestrial Reference System(TRS) is defined with its origin at the same position as the ECI System. The z axis is equal to the Conventional Terrestrial Pole (CTP). The x_e^i axis points at the intersection of the Greenwich Mean Meridian and the equator. A practical implementation of this system goes under the name (conventional)Terrestrial Reference Frame(TRF). One commonly used implementation is the World Geodetic System 84 (WGS-84).

2.1.3 Body Frame

The body frame is what the satellite orientation is described with. All measurements taken from the satellite happens from this frame and the effect from all forces the satellite experiences may be described for this frame with respected to the ECI frame. The frame is positioned at the satellite center of mass with axes pointing in the directions of the satellite coils. The z^b axis points in the direction of the coil with the smallest area while the y^b and x^b axes points in the directions of the two coils with largest surface area. This definition was chosen because it is easily recognized on the satellite without further markings.

2.2 Temperature Variations

The NUTS CubeSat uses an experimental frame where the inner panels are made from carbon fiber. The carbon fiber panels are expected to have much lower thermal conductivity compared to the more common aluminum frame. This makes estimates and reports of specific temperature readings from other CubeSat projects less comparable to the NUTS project. But we will assume that the dynamical nature of temperature changes will be similar. For this reason information on the temperature variations from the Compass-1 CubeSat is presented. A thermal analysis and a detailed post flight report on measured temperatures is available for the Compass-1 satellite.

2.2.1 Thermal analysis

Design of the Thermal Control System for Compass-1 [Czernik \(2004\)](#) perform initial 2D and 3D analysis of max and min temperatures at the end of sun and shadow orbit phases. For the 3D simulation with heat dissipation from internal electronics, 5 surfaces were covered with 30% black paint and 70% solar cells while the side with antennas is 100% black paint. 60.5 min of the orbit is spent in the Sun while 35.3 is spent in shadow. End of Sun phase values are from 11.8 deg C to 18.2 deg C on the outside surfaces. Reading temperature values from figures is a little challenging but they seem to range between 11.3 deg C and 20.0 deg C for components inside the satellite. During the shadow phase outside temperatures range from -41.7 deg C to -43.5 deg C while inside component temperature range from -9.8 deg C to -43.4 deg C

2.2.2 Post flight report

The COMPASS post flight report [Scholz et al. \(2010\)](#) state that the active thermal control device was turned off because it caused a malfunction of the satellite. Normal operating conditions was

regained and at this point only the passive thermal control techniques are in effect. The Passive techniques employed were rooted in the assumption that satellite temperatures would be cold rather than hot. The back/inn side of panels were painted black to radiate into the cube and electronics boards were given limited thermal conductive contact to satellite structure.

The inside electronics boards EPS, RTC, ADCS and inside surface of sun sensor board temperatures are also plotted from 7/31/08 to a little past 1/7/09. Over this time period it can be seen that electronics board temperature increases by approximately 5 degrees due to increased solar flux at winter solstice. The temperature range at the end of the plot is from a less than -5 deg C to mostly below 25 deg C with some peaks around 30 deg C . Sun sensor panel temperatures are recorded between $-30\text{ to }40\text{ deg C}$.

In [Scholz et al. \(2010\)](#) fig22 the temperature of panels and the ADCS is plotted over several orbits with time stamps. The temperature variations described in the paragraph above can be seen in more detail here and for later use an approximate orbit time can be observed to be 114 min .

An instance of the de-tumbling phase is plotted over a 60 min period with ADCS board and panel temperatures in [Scholz et al. \(2010\)](#) fig23. It can be seen here that ADCS board temperatures are much more constant during de-tumbling and falls slightly slower than panel temperatures when the satellite moves into shadow. Of particular interest is the length of a shadow phase and the ADCS temperature gradient. If we use the moment when panel temperature dynamics sharply changes, slightly after 1500 sec and after 3500 sec we get a shadow phase time approximately 34 min long. On this plot the ADCS temperature changes from 20°C to 0°C in the time period from 2000 sec to 3500 sec giving a gradient rounded up to -0.014°C/s .

While off topic it is also worth mentioning that orbit estimation was done successfully based on uploaded UTC time and general orbit parameters, the same method is implemented on the NUTS CubeSat.

2.3 Satellite Irradiance

We need our satellite to measure a sun vector. Most Sun sensors usually come as a stand alone photo diode or arrangement of several photo diodes depending on the type used. These only measure a specific part of the radiance specter experienced by the satellite. Therefore we will here investigate the spectral radiance from the Sun and Earth. As reference material for this section "Weather Modeling and Forecasting of PV Systems" [Paulescu et al. \(2012\)](#) has been found convenient and detailed. If other sources are used they will be mentioned specifically.

2.3.1 Radiance, Irradiance, and Reflected light

The necessary basic terms, definitions and approximations used to describe quantities of light is introduced here, the reference source used for this material is [Ryer \(1998\)](#) and [Burle \(2000\)](#). The first is radiant flux given as photons per second [p/s] or watt [W]. The relation between them is given bellow

$$\Phi = \left(\frac{p}{s} hc \right) [W] \quad (2.1)$$

where h is Planck's constant ($6.623 \cdot 10^{-34}$ [Js]) and c is the speed of light ($2.998 \cdot 10^8$ [m/s]). Radiant flux is the total flux exiting or entering a source.

When we talk about light at a surface it is often as irradiance when it enters/hits something (E) or radiant exitance (M) when it leaves a surface. They are both flux density defined as follows.

$$E = \frac{\partial \Phi}{\partial A} [W/m^2] \quad (2.2)$$

$$M = \frac{\partial \Phi}{\partial A} [W/m^2] \quad (2.3)$$

Irradiance in most cases is reduced by distance because it spreads outwards over the surface of a sphere from its source. To get irradiance at some distance and direction in relation to a surface source, radiance (L) is the theoretically most correct place to start. It is a directional measure of light independent of distance because it is defined as: Flux per projected area ($A \cos(\theta_{ze})$), per steradian (Ω). Where θ_{ze} is the angle of incident or leaving light (depending on its use) with respect to surface normal often termed the zenith angle. In the equation below it is for light leaving a surface.

$$L = \frac{\partial \Phi}{\partial \Omega \partial A \cos(\theta_{ze})} [W / sr / m^2] \quad (2.4)$$

The unit steradian (sr) or solid angle quantifies a fraction of a spherical surface and is defined as given under. A is the surface area of the sphere where light of interest is radiated into and d is the distance, perpendicularly from the projected surface to a target.

$$\Omega = \frac{A}{d^2} \quad (2.5)$$

When the distance to the target is at least 10 times larger than source radius the surface can be approximated as a point source. For such cases irradiance can be found from flux per steradian (I) multiplied with the inverse of d^2 .

$$I = \frac{E}{d^2} [W / sr] \quad (2.6)$$

This property also comes in the form

$$E_1 = \frac{d_2^2}{d_1^2} E_2 \quad (2.7)$$

where E_1 and E_2 are irradiance at distances d_1 and d_2 from the source. As shown earlier radiance is a directional quantity and radiance will in most cases change with the direction. With Earth as a highly irregular surface this often complicates calculations therefore Earth is often approximated as a perfect diffuse reflector, a Lambertian surface.

The total flux in a direction from a Lambertian surface of area A will be proportional to $A \cdot \cos(\theta_{ze})$. For this very reason radiance is actually constant with respect to viewing direction and from exitance it can be found using the equation below.

$$L = \frac{M}{\pi} \quad (2.8)$$

Where π is the result of integrating $\cos(\theta_{ze})$ over the steradian of a half sphere.

Amongst many forms of reflection is specular, spread, diffuse and combinations of these. For complex surfaces, a bidirectional reflectance distribution function (BRDF) is used. In seen literature on reflection of light from Earth the irradiance is usually split into diffuse and beam/direct.

2.3.2 Sun Irradiance

When talking about Solar radiance it is usually at a coefficient of relative distance traveled through the atmosphere AM(air mas) approximated as given in equation 2.9

$$AM = \frac{1}{\cos(\theta_{sz})} \quad (2.9)$$

AM1 is considered radiance passing through one atmosphere defined as the path from top, down to sea level at zenith angle θ_{sz} . This approximation seems to be good until light bends in the atmosphere, a effect substantial for zenith angles larger than 80° .

Before the Sun hits atmosphere we have incident light at AM0 or extra terrestrial radiance(ETR). Usually when one talks about the power of ETR it is the best estimate of a average solar constant $E_{AM0} = 1366.1 W/m^2$. During a year this value will fluctuate around E_{AM0} with 6.9% from $1423.0 W/m^2$ to $1321.0 W/m^2$ because earths orbit is not circular.

A standard AM0 spectral radiance from the Sun is given in fig 2.1 for the purpose of calculating max current output from sun sensors later. The specter is generated using the SMARTS2.95 software [Gueymard \(1995\)](#) [Gueymard \(2001\)](#)

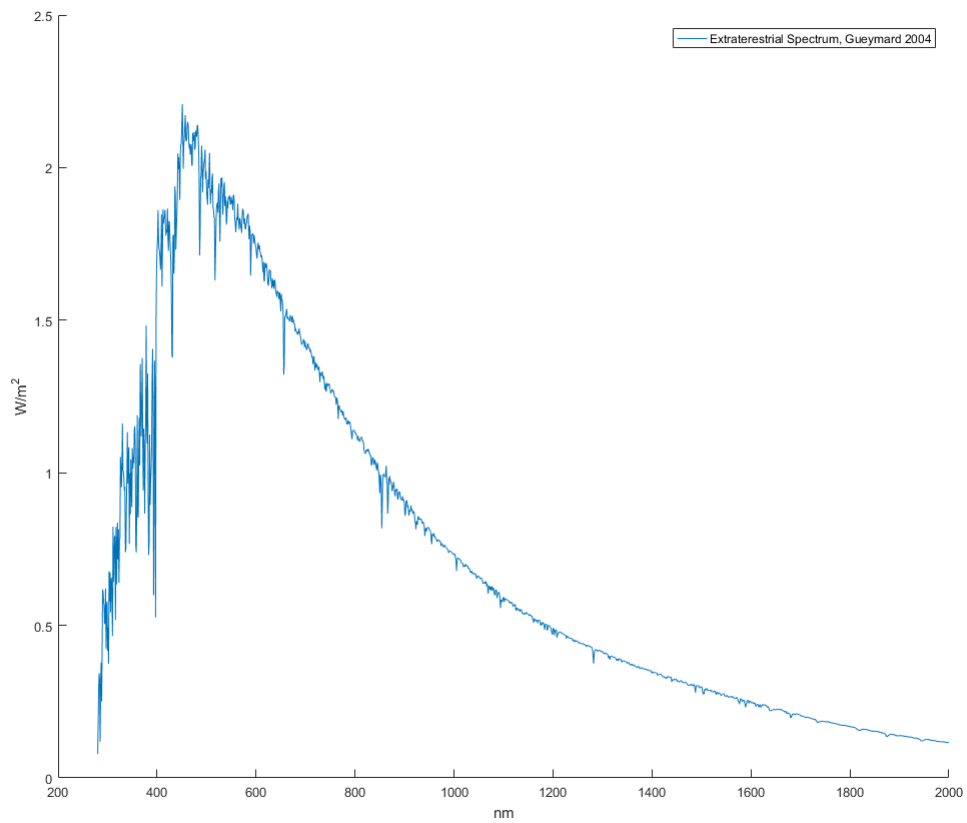


Figure 2.1: Data used to create this plot was acquired using the SMARTS2.95 software [Gueymard \(1995\)](#) [Gueymard \(2001\)](#) with a solar constant of 1366.1 irradiance

2.3.3 Earth Irradiance

A interfering problem when measuring a Sun vector is reflect light from earth at top of the atmosphere (TOA). After the atmosphere earth system absorbs and scatters large parts of irradiated power, TOA earth reflected light usually lies somewhere around 30% of Sun radiance. Therefore we will here try to cover basic background material related to experienced TOA Earth radiance and calculations of incident light intensity.

Light Radiation Model For Earth

Form "Weather Modeling and forecasting of PV systems Operation" [Paulescu et al. \(2012\)](#) several models used to extract ground level radiation from satellite observations are given. The Janjai model developed for tropical environments is briefly summarized. It gives an overview of what approximately happens to light in its course from space to the surface of earth and back to a satellite. This description is repeated under together with an illustration taken from the book.

As light first enters the atmosphere part of it is scattered back by air molecules and clouds. This is represented with parameters for cloud atmospheric albedo ρ_A and aerosols ρ_{aer} . Further more light is absorbed by ozone, mixed gases, water vapor, and aerosols represented respectively with absorption coefficient α_O , α_g , α_w and α_{aer} . The remaining part is reflected at ground level by the coefficient ρ_g . On the way back up this model considers most of what can be absorbed by the atmosphere as already absorbed. Therefore the process is not calculated twice, while the reflection part ρ_A and ρ_{aer} happens again but this time, back down.

Thus we have that extraterrestrial albedo ρ_{EA} detected by a satellite can be expressed as

$$\rho_{EA} = \rho_A + \rho_{aer} + (1 - \rho_A - \rho_{aer})^2 (1 - \alpha_0 - \alpha_w - \alpha_g - \alpha_{aer}) (1 - \alpha_{aer}) \rho_g \quad (2.10)$$

Earth Spectra's

As a result this model gives many different radiance spectra's depending on atmosphere-Earth conditions such as clouds, aerosol pollution, the amount of H^2O in the atmosphere and different types of surfaces for example deserts, ice and oceans. "Exploring the Changing Earth's Atmosphere" by [Gottwald and Bovensmann \(2010\)](#) details the SCIAMACHY spectral radiance measurement mission aboard ENVISAT. SCIAMACHY measures earth spectral radiance while pointing in directions nadir and limb(tangent with earths surface), at the spectral regions UV-VIS-NIR and SWIR.

Of particular interest in this book is figure 7.7 from [Gottwald and Bovensmann \(2010\)](#) of the Earth reflectance spectra. Found here in figure 2.2. In the book this figure is a example given to illustrate what is needed to calculate properties of trace gases, aerosols, clouds and surface parameters from the SCHIAMACHY insturment measurements.

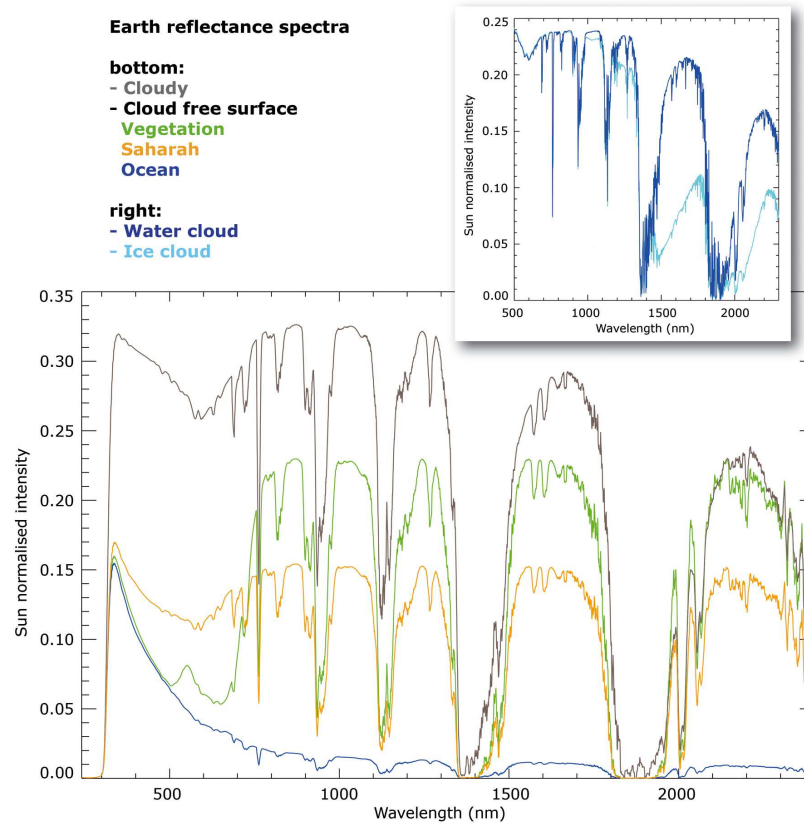


Figure 2.2: Earth reflectance spectra (Sun normalised intensity) for various cloud and surface conditions. The inset shows the variation in the reflectance spectrum due to changes in the thermodynamic state of water in the cloud from liquid water to ice. The large difference in reflectance spectrum around 1600 nm for ice and water clouds is used to derive information on the thermodynamical state of water in clouds (Courtesy: IUP-IFE, University of Bremen). figure 7.7 in [Gottwald and Bovensmann \(2010\)](#)

For this thesis the reflectance spectra serve as a good example on how these spectra change under different conditions. The significant reductions in reflectance around 900[*nm*], 1100[*nm*], 1400[*nm*] and 1900[*nm*] caused by H^2O in the atmosphere may be used to avoid Earth reflectance with an appropriate choice of photodiode. This possibility will be revisited in section 3.2 where photodiodes for a simple Sun sensor is chosen.

A attempt at generating TOA reflectance spectra using, equation 2.11 from [Gottwald and Bovens-](#)

mann (2010) is also presented bellow. Equation 2.11 is given here with slightly different notation. L_{ea} is Earth and atmospheric radiance hitting the satellite, E_{et} is solar or extra terrestrial irradiance hitting earth at TOA.

$$R_{ea} = \pi \frac{L_{ea}}{E_{et}} \quad (2.11)$$

Data used to make the specter was acquired with SMARTS2.95 output: Atmospheric reflectance R_a , Gueymard 2004 AM0 Sun specter E_{et} , upward hemispheric ground reflected irradiance E_{ugr} and beam radiation transmittance T_b . As shown in equation 2.12 bellow and reasoned for afterwards based on the Janjai model and preceeding theory.

$$E_{ea} = E_{et}R_a + T_bE_{ug} \quad (2.12)$$

$$E_{ea} = E_{ar} + E_{er} \quad (2.13)$$

Upward hemispheric ground reflected irradiance E_{ug} is used as the remaining Sun light after atmospheric scattering, absorption and ground reflectance as described above by the Janjai model.

Earth reflected radiance E_{er} is generated from I_{ug} by multiplication with T_b . While the Janjai model only takes atmospheric reflectance to the most significant source of reduction upwards it is believed that using the transmittance is not incorrec to any significant deggre in this thesis.

Atmospheric reflected irradiance E_{ar} was generated by multiplying the Sun spectra given above in figure 2.1 E_{et} with atmospheric reflectance R_a .

The resulting reflectance found E_{ea}/E_{et} can be seen in figures 2.3 and 2.4 where different SMARTS2.95 setting have been used to generate the spectra used in equation 2.12. For the figures 2.4 and 2.3 as a comparison the Sahara Earth and vegetation Earth reflectance was extracted from figure 7.7 in [Gottwald and Bovensmann \(2010\)](#) using the Graph digitizer [Rohatgi \(2011\)](#) and plotted in respective figures labeled as "SCHIMACHY Dessert" and "SCHIMACHY Vegetation". The attempt at creating a similar reflectance spectra for a dessert and a type of vegetation is also plotted in these two figures labeled with SMARTS2.95 settings

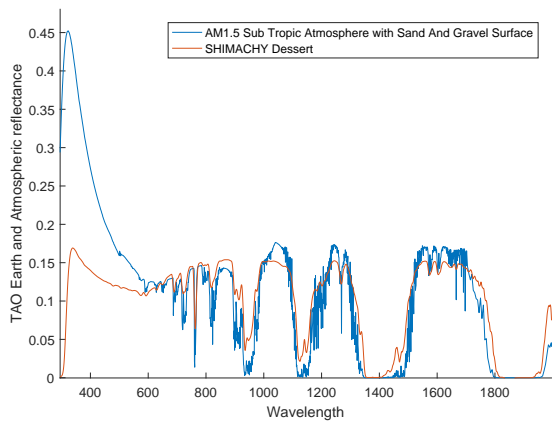


Figure 2.3: The blue line is the reflectance spectra generated here using equation 2.12 and 2.11 together with SMARTS2.95 [Gueymard \(1995\)](#), [Gueymard \(2001\)](#) generated data. SMARTS settings are in the blue label. SCHIMACHY Dessert is Sahara reflectance extracted from figure 7.7 in [Gottwald and Bovensmann \(2010\)](#) using the Graph digitizer [Rohatgi \(2011\)](#)

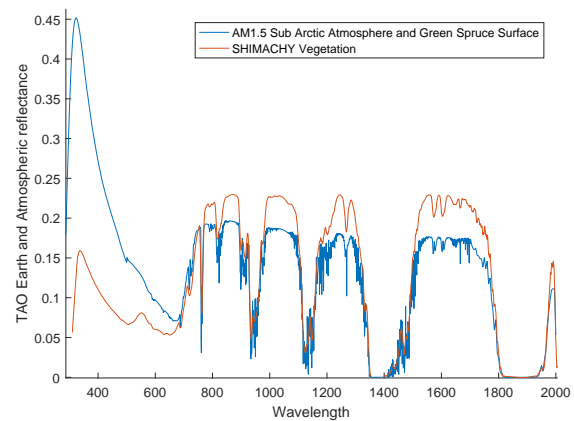


Figure 2.4: The blue line is the reflectance spectra generated here using equation 2.12 and 2.11 together with SMARTS2.95 [Gueymard \(1995\)](#), [Gueymard \(2001\)](#) generated data. SMARTS settings are in the blue label. SCHIMACHY Vegetation is Vegetation reflectance extracted from figure 7.7 in [Gottwald and Bovensmann \(2010\)](#) using the Graph digitizer [Rohatgi \(2011\)](#)

Clearly this author has completely failed to generate ultra violet(UV) reflected light that is mostly reflected from the atmosphere E_{ar} in this case. Other than the UV reflected light the fit seems

to be reasonably good. But it must also be mentioned that while the AM1.5 sub arctic atmosphere and green spruce from Norway fits reasonably well a AM1 US standard atmosphere with green grass as Earth surface would not fit the vegetation spectra at all. And vegetation spectra is most likely a average from different types vegetated area, not the reflectance spectra of Norwegian green spruce with sub arctic atmosphere. It can therefor not be concluded from these comparisons that the method used here to make the reflectance spectra is reasonable because the reasonable fit may be random. Also this author dose not in any way believe he understands this topic well enough that such a thing can be claimed. But the exercise was interesting and is hopefully so for any reader as well. It is also worth mentioning that the effect of T_b is very small on the result just as stated for the Janjai model. From this authors experience the SMARTS2.95 is simple to use bu seems to be focused on Irradiance values after Earths atmosphere and may be more appropriate for such use. Other software that may be better for TOA spectra also likely to be more complicated in use and not free, is the MODTRAN®5 software, <http://modtran5.com>.

2.3.4 Earth Reflection Model

Earth reflectance as observed by a satellite as shown previously in figure 2.2 varies significantly with surface composition. Therefore a model more accurate than an average reflectance from a spherical surface is desirable. One such model was made by [Bhanderi and Bak \(2005\)](#) and will be presented here.

The model is based on a map of reflectivity data recorded by the Earth Probe Satellite of the TOMS project. The satellite in question provides available data from 1996 to 1997 at an altitude of 515km before the orbit was raised to 740km.

The disadvantage of using TOMS data is the assumption of Earth reflectance at 360nm being approximately the same for all wavelengths. This is not necessarily true, see figure 2.2. TOA reflectance from oceans is close to zero approximately after 500nm, sensors with sensitivity at higher wavelengths is expected to receive significantly less irradiance from Earth in real life than what TOMS data would imply.

A big advantage is that Bhanderi has made and hosts on his home page a AlbedoToolbox and data TOMS data from 1996-2005 converted for use in Matlab with said toolbox. The tool is naturally based on the model from [Bhanderi and Bak \(2005\)](#) that will be presented here.

The model calculates a reflected irradiance at a satellite for each cell c of reflectance $\rho_c(\phi_{lat}, \theta_{long})$. Naturally the position of ρ_c is in the ECEF frame where all other vectors will also be in this subsection. ϕ_{lat} and θ_{long} are at the center of each cell area $A_c(\phi_{lat})$. Subscript c will indicate that vectors and values are functions of ϕ_{lat} and/or θ_{long} when this is natural. Finally the first equation starts with flux received Φ_c per cell as given below.

$$\Phi_c(\phi_{lat}, \theta_{long}) = E_{AM0} A_c(\phi_{lat}) \{ \mathbf{r}_{sun}^T \mathbf{n}_c \}_0^\infty \quad (2.14)$$

\mathbf{r}_{sun} and \mathbf{n}_c are here unitvectors giving Sun direction from Earth and cell normal. Together they give fraction of surface area seen from the Sun with lower limit indicated by $\{\}_0^\infty$. Following this expression total flux reflected $\Phi_{c\rho}$ per cell is simply.

$$\Phi_{c\rho}(\phi_{lat}, \theta_{long}) = \rho_c \Phi_c \quad (2.15)$$

For small surfaces and large distances, dividing $\Phi_{c\rho}$ by π and $d_{sat,c}^2$, gives irradiance at satellite distance $d_{sat,c}$ from the cell,

$$E_{c\rho,d}(\phi_{lat}, \theta_{long}) = \frac{\Phi_{c\rho}}{\pi d_{sat,c}^2}. \quad (2.16)$$

The fraction of cell area visible from the satellite is taken into account as with the Sun, where $\mathbf{r}_{sat,c}^T$ is a unit vector pointing from cell to satellite

$$E_{c\rho,sat}(\phi_{lat}, \theta_{long}) = E_{c\rho,d} \{\mathbf{r}_{sat,c}^T \mathbf{n}_c\}_0^\infty \quad (2.17)$$

The expression can also be written using the condition of visible cells from the Sun and satellite by the intersection of subsets $V_{sun} \subset C$ and $V_{sat} \subset C$, from the complete set of Earth map cells C

$$E_{c\rho,sat}(\phi_{lat}, \theta_{long}) = \begin{cases} E_{c\rho,d} \mathbf{r}_{sat,c}^T \mathbf{n}_c, & \text{if } (\phi_{lat}, \theta_{long}) \in V_{sun} \cap V_{sat} \\ 0, & \text{otherwise} \end{cases} \quad (2.18)$$

2.4 Sun Sensors

Dieffent types and arrangements of photodiodes can give many types of sun sensors. Those most commonly seen implemented on cubesats use PIN, position sensitive and quadrant photodiodes. Theory and history found on these three methods will be presented here. The subsections will first give short descriptions of Sun sensing methods related to the innstrument before advantages, disadvantages and some relevant satellite history.

2.4.1 PIN Photodiodes

A Sun vector can be attained under the conditions of having at least three PIN photodiodes oriented with:

- Sensor normals linearly independent to each other.
- Overlapping field of view(FOW).

This instrument is often termed pyramid sun sensor. A vector of irradiance \mathbf{s} , for example from the Sun of intensity E_{AM0} can be mapped to photodiode current output I_{pi} for photodiodes $i = 1 \dots n$ following.

$$I_p = H_{Kn} \mathbf{s}_i^b \quad (2.19)$$

$$\begin{bmatrix} I_{p1} \\ I_{p2} \\ \vdots \\ I_{pn} \end{bmatrix} = \begin{bmatrix} K_{R1} n_{p1} \\ K_{R2} n_{p2} \\ \vdots \\ K_{Rn} n_{pn} \end{bmatrix} \begin{bmatrix} s_x \\ s_y \\ s_z \end{bmatrix} G_{sc} \quad (2.20)$$

Where n_{pi} is a vector normal to photodiode, i sensing surface. This works when photodiode angular sensitivity follow the ideal lambertian cosine law. In other words current output is proportional to $\cos(\theta_z)$ where θ_z is the zenith angle to incident light. K_{Ri} is a conversion factor to current from irradiance for the specific photodiode. A example of this propertie being used can be found in [Springmann \(2013\)](#)[Bhanderi and Bak \(2005\)](#).

Relevant characteristics and theory on the conversion from irradiance to currnt is given bellow. Unless specifically mentioned or the information is repeated it is based on the application sheet "Photodiode Characteristics and Applications"[OSI](#)

Material: PIN Photodiodes can be made with many different types of materials that affect several properties of photodiodes such as responsivity with respect to wavelength(λ) bandwidth. Silicon materials give reponsivity in the aproximate range of $200nm$ to $1100nm$. Indium gallium arsenide(InGaAs) PIN photodiodes give responsivity in the aproximate range $1000nm$ and above $2000nm$.

Spectral Responsivity: This is the ratio of short circuit current to total incident flux/light power at a given wavelength. It is often referred to as photocurrent when used in photovoltaic mode. $R(\lambda)[A/W]$ gives photo current $I_p(\lambda)$ for incident flux $\Phi(\lambda)[W]$. Following the equations,

$$I_p(\lambda) = R(\lambda)AE(\lambda) \quad (2.21)$$

$$I_p(\lambda) = R(\lambda)\Phi(\lambda) \quad (2.22)$$

where A is the photo sensitive area.

Relative Spectral Sensitivity This is a percentage of incident irradiance per wavelength $S_R(\lambda)$. It is often given in data sheets together with R_λ , responsiveness for a specific wavelength. They are a result of both the material used for the sensing surface and the filter in the packaging. With respect to $R(\lambda)$ it is here assumed that it can be expressed as follows.

$$S_R(\lambda) = \frac{R(\lambda)}{R_{\lambda,max}} \quad (2.23)$$

Relative Angle Sensitivity: This is usually given as a change in sensitivity($S_A(\theta_z)$) in the range 1.0 to 0.0 for a angle of incident light θ_z with respect to sensor normal n_{pi} . The best possible characteristic for this application is naturally lambertian.

$$S_A(\theta_z) = \cos(\theta_z) \quad (2.24)$$

As shown in the polar plot of Fig. ... This propertie is heavily affected by the lense used in potodiode packaging.

Lenses and Filters: Photodiodes often come packaged in lenses and optical filters that greatly affect the angle incidence sensitivity, field of view and responsivity. Additional band pass filters can be bought separately for any desirable wavelength.

Rise/Fall Time: It is the time required for the photodiode to change between 10% and 90% of final output. Several factors affect the rise/fall time, but it is observed to typically be in the order of nanoseconds to microseconds. Our application is so slow that it is considered to be irrelevant.

Noise-equivalent power: (NEP) is the incident light power required to generate a photocurrent I_P equal to noise current I_{ns} .

$$NEP = \frac{I_{ns}}{R_\lambda} \quad (2.25)$$

Total Noise This is a sum of shot noise I_{sn} and thermal/johnson noise I_{jn} . Shot noise is statistical variations of total current in the photodiode ($I_P + I_D$) expressed as rms noise. Δf is measurement bandwidth and q is electron charge. Johnson noise is most dominant in photovoltaic mode and is a characteristic of photodiode shunt resistance, in general it is

a propertie of all resistors. k_b is the Boltzmann Constant, T is absolute temperature in Kelvin and R_{sh} is shunt resistance.

$$I_{tn} = \sqrt{I_{sn}^2 + I_{jn}^2} \quad (2.26)$$

$$I_{sn} = \sqrt{2q(I_P + I_D)}\sqrt{\Delta f} \quad (2.27)$$

$$I_{jn} = \sqrt{\frac{4k_B T}{R_{sh}}}\sqrt{\Delta f} \quad (2.28)$$

Temperature Coefficient: TC_I [%/K] is the percentage change in responsivity per Kelvin(K).

For relevant photodiodes this coefficient has been observed to range from 0.1 – 0.03%/K on seen data sheets. To simplify notation it is here written as.

$$C_T(K) = TC_I \times K \quad (2.29)$$

It should also be mentioned that this coeficient is in reality not constant with respect to wavelength.

Total current out of a photodiode is the sum of photocurrent I_P and dark current I_D as mentioned previously. They are expressed as follows.

$$I_P = R_\lambda \Phi_\lambda \quad (2.30)$$

$$I_D = I_{SAT} \left(e^{\frac{qV_A}{k_B T}} - 1 \right) \quad (2.31)$$

Where V_A is voltage over the photodiode and I_{SAT} is reverse saturation current.

Advantages

The advantages of this solution is its simplicity. Minimal amount of components needed, 6 photodiodes. One opamp circuit and ADC per photodiode to get 4π steradian/full attitude sphere FOW on the Sun sensor. More than 6 are needed if individual photodiode FOW is less than 180deg. For this particular case photodiodes are mounted on each side of the satellite. The low number of components makes this solution more robust and easier to implement with redundancy.

Disadvantages

The disadvantages are many. Only coarse angular accuracy on the order of 10^0 deg has been achieved [Shafer et al. \(2008\)](#). Only 90deg of the FOV is used for measurement in the traditional mounting directly on Cube Sat surfaces while incident light is accepted from 270deg for all the photodiodes combined. This makes disturbances from other light sources such as Earth more significant compared to other alternatives.

For this reason many implementations use a higher number of photodiodes or similar sensing elements tilted/oriented to reduce FOW accepting incident light while increasing Sun vector sensing FOW.

NanoSat-1B

Here three pyramids are mounted with normals along negative, positive y axis, and positive z axis body frame. Each pyramid has 5 solar cells. From each pyramid Sun sensor a 160deg FOW was used and a accuracy of 1.8deg was achieved. Large increase in accuracy comes from

choosing groups of 3 cells with more orthogonal normal vectors. A lesser increase in accuracy was gained from cell orientation/normal vector calibration in orbit [Ortega et al. \(2010\)](#).

Reflection of light from the cells is a known error source with respect to the ideal lambertian model often corrected with fourth order polynomials or large tables with correction factors. Another simpler method is introduced by [Ortega et al. \(2010\)](#).

$$I(\theta_z) = (I_{MAX} - I_0)\cos(\theta_z) + I_0 \quad (2.32)$$

Where I is current generated by solar cells and I_0 is a constant. This method preserves the linearity in equation 2.20.

Radio Aurora Explorer(RAX) 1 and 2

RAX 1 and 2 are cube satellites [Cutler et al. \(2011\)](#) using Sun sensors similar to NanoSat-1B [Springmann and Cutler \(2014\)](#). They use photodiodes from OSRAM SFH2430 angled with one ramp per photodiode. It is stated that degradation due to UV radiation is a known problem with photodiodes and is suspected to be the reason for degradation of sensitivity reported on RAX 1. The issue was reduced on RAX 2 with coverglass using the same coating used to protect solar cells. The Photodiode array consist of 3 on the top and side panels($\pm x$ and $\pm y$ axis) and 2 on the bottom panel($-z$ axis). Side panel diodes are mounted on ramps oriented for optimal accuracy in measurement of Sun direction independent of satellite orientation. Calibrations gave a improvement of Sun sensor accuracy of 10 deg and attitude accuracy bellow 1 deg was achieved. Calibration of sensitivity/scalefactor and alignment/orientation is done using a Multiplicative Extended Kalman Filter and the model of Earth albedo [Bhanderi and Bak \(2005\)](#) to correct measurements, same model as used in this thesis.

Colorado Student Space Weather Experiment(CSSWE)

Very little information is given in [Gerhardt et al. \(2013\)](#) on orientation of photodiodes and the type used on on this cubesat. But illuminance is used for measured intensity so one can assume that photodiodes detecting visible light was used(similar to RAX). It is mentioned that 4 are mounted on x an y panels. The interesting part is the plot of maximum measured illuminance from photodiodes showing sever reduction from mid September to March. The plot indicate fast degradation of sensitvty to almost half of initial values. This is attributed to UV radiation darkening photodiode packaging plastic without any proof or citation. At the edge of the South Atlantic Anomaly all devices on housekeeping I2C lines stopped responding mid October. After a reboot response was not regained from one ADC, and 1-3 bits on two other 8-bit ADCs stopped functioning. This is visible on figures presented in the article.

2.4.2 Position Sensitive Diode(PSD)

Two dimensional Position sensitive diodes are usually of sizes around $10 \times 10mm - 2 \times 2mm$ and gives 4 analog signals that together represents a position of illumination on the sensor. Placing a cover with a pinhole above the sensor allows for calculation of incident angle from the position of the light spot created by the pinhole. In [Shafer et al. \(2008\)](#) this resulted in a FOW of $120deg$, an absolute accuracy of approximately $0.5deg$ and a steady state error of $0.05deg$ with PSD of area $10 \times 10mm$.

From application note [PSD](#) from OSI Optoelectronics possible measurement circuitry is expected to involve at least 4 opamps transforming current to volt before sampling and calculation of position. There are two main types of PSD's. The duo-lateral has lower position error and practically perfect position linearity compared to the tetra-lateral that exhibit higher non-linearity further away from center. Position calculation for both is done using the following equations.

$$x = \frac{(I_{x+} - I_{x-}) L_x}{(I_{x+} + I_{x-}) 2} \quad (2.33)$$

$$y = \frac{(I_{y+} - I_{y-}) L_y}{(I_{y+} + I_{y-}) 2} \quad (2.34)$$

Where $L_{x/y}$ and $I_{x/y\pm}$ is the PSD length and photocurrent measured on positive and negative sides of the PSD as defined by the designer of the sensor.

Advantages

While light intensity will affect the signal to noise ratio, position calculations are completely independent of it. As a result most of the error sources directly related to finding incident angle

with cosine sensors is removed and calibration is expected to be a lot simpler. In addition the error source, albedo from Earth is likely a lesser problem because FOW accepting light is equal to FOW that can give a sun vector. It is also much simpler to reduce the FOW with these sensors making them ideal for fine orientation measurement in a limited FOW

Disadvantages

The biggest disadvantage with PSD's is the amount of resources required. As an example a implementation to cover the entire attitude sphere would need 6 sensors, 24 op-amps and ADC conversions. ADC's could be reduced to 12 if analog summation are done with a increased number of opamps to 42. These are also significantly more expensive than other alternatives with a price tag off around 200\$ or per PSD. Design of the aperture with pinhole and appropriate operational amplifier cricuites is also needed because a complete solution has now been found.

2.4.3 Quadrant Photodiodes

This sensor works under the same principle as the PSD but uses four separate photocells mounted close together such that a light spot partially covers all the cells. Output current from the four cells gives position and consequently calculated in a similar fashion to PSD.

Advantages

Advantages consist of a significantly lower price tag than PSD's and Solar MEMS [Sol](#) can deliver these with the square opening and voltage output of the four diodes as a compact device suitable for making a Sun sensor simplifying the work involved in sensor design compared to a PSD.

Disadvantages

In [Shafer et al. \(2008\)](#) significant drawbacks mentioned is nonlinearity in the photodiodes response and as a result the requirement of a look-up table to achieve greater than 2 degree accuracy. The photodiodes response are also said to change slowly over time which would require additional tuning while in operation.

With respect to opamps and ADC needed, the situation is similar to PSD's. The difference is that this involves 4 separate sensing elements that may change differently over time. Thus digital summation and a more ADC's vs opamps may be an advantage.

2.5 MEMS Gyroscope Errors

To reason for and improve on our current choice of gyroscope on the CubeSat, intuitively it seems correct to find knowledge on Coriolis Vibratory MEMS gyro error models. It is expected that this will allow us to interpret data sheets more correctly and judge which errors are going to be simpler to deal with. All error sources on gyroscopes are not mentioned on data sheets thus this is expected to show the limitations present in use of datasheets to chose sensors.

$$\tilde{\omega} = (I + \delta S_G + M_G)\omega + B_G + \epsilon_G \quad (2.35)$$

From what has been seen this is the usual basic error model known to most people. Errors in equation 2.35 is almost always present in they're simplest linear form.

δS_G : Scale factor errors.

M_G : Missalignment and Cross-coupling/Orthogonality errors.

B_G : Bias, or zero rate error is independent on rotation velocity, usually slow but far from always and is both random and deterministic.

ϵ_G : White noise

Most of the more specific/precise parameters can usually be sorted into the three first categories/types of error. For example scaling errors also involve nonlinear, random and temperature dependent terms, while bias may involve a constant term, temperature and acceleration dependent terms.

Comprehensive detailed error models specifically for MEMS gyroscopes has been hard to find. For conventional gyroscopes, errors and models are well known and described in Strapdown Inertial Navigation Technology(SINT) [Titterton and Weston \(2004\)](#). These errors involve those mentioned above plus the following described very shortly.

In the category of bias there is acceleration proportional, ansioelastic and ansioinertia errors. Ansioelastic and ansioinertia errors around a axis are proportional to the product of acceleration or angular rates respectively, along or around the two remaining orthogonal axes. Extra rotation dynamics problems involve, angular acceleration proportional errors.

For these error sources strapdown inertial navigation technology state that all or some of the following subcomponents will be present

- Turn-on to turn-on error that varies from one instance of gyroscope power on to another.
- In-run error that randomly changes while the gyro is powered on.
- Temperature induced variations.
- A fixed or repeatable and always present non-changing component.

The error model from SINT is mentioned because MEMS Coriolis vibratory gyroscopes operate under the same principles as Vibratory gyroscopes, and SINT states that a similar form may be appropriate for these. Those few errors mentioned specifically for MEMS will be talked about later

A different option can be found from "How Good Is Your Gyro?" [Grewal and Andrews \(2010\)](#) here a general purpose equation is given as shown under. Instead of ansioelastic and ansioinertia errors, second order coupling errors(b_{xx}, b_{xy}, b_{xz}) are present, inconveniently with the symbol used for bias. Subcomponents mentioned in SINT are also mentioned here.

$$\tilde{\omega}_x = (s + \delta s)\omega_x + b_x + b_{gx}a_x + m_y\omega_y + m_z\omega_z + b_{xx}(\omega_x)^2 + b_{xy}\omega_x\omega_y + b_{xz}\omega_x\omega_z + v_x \quad (2.36)$$

Moving on from the general case, the MEMS gyroscope errors believed to be most significant are thermal and stochastic errors and will therefore be focused on. It can be assumed that linear accelerations, vibrations and angular accelerations will be minuscule for the satellite. If information on the assumed minuscule errors are accidentally found it will be included if they are big under gravity. The information is sorted as sub components of scale factor, misalignment and bias when possible.

2.5.1 Scale Factor(δS_G)

$$\delta S_G = \begin{bmatrix} \delta s_x & 0 & 0 \\ 0 & \delta s_y & 0 \\ 0 & 0 & \delta s_z \end{bmatrix} \quad (2.37)$$

Run-to-Run\Turn on Error: Is the initial scale error that changes from power on to power on. It is constant during a run and can be seen under constant operating conditions. This is part of a repeatability problem present in MEMS gyroscopes not reported by manufacturers [Titterton and Weston \(2004\)](#) [Aggarwal \(2010\)](#).

Temperature dependant In ref [Aggarwal \(2010\)](#) it is stated that scale errors can be found as one part deterministic error that change with environmental factors, and can to a degree be modeled as a temperature dependent parameter. In "Fast Thermal Calibration of Low-Grade Inertial Sensors and Inertial Measurement Units" [Niu et al. \(2013\)](#) scale factor errors are shown to change with at most 1.1% from $-10C$ to $70C$. To compensate for the errors third order polynomials was used with great success reducing the effect to 0.15%

Acceleration dependent In "Analysis of compensation for g-sensitivity scale-factor error for a MEMS vibratory gyroscope" [Park et al. \(2015\)](#) it is shown that change in scale factor may be proportional with accelerations perpendicular to a axis of rotation. A experiment was performed for accelerations from -30 to $30g$, applied along the y axis with rotations around x up to and above $500deg/s$. It should also be mentioned that plots where also shown with accelerations along axes without rotation speeds and those bias changes seen if any are well bellow $5deg/s$. The results gave a highly linear relation with acceleration/gravity dependent scale factors around 0.06%

2.5.2 Misalignment Error (M_G)

Or cross axis error is caused by non orthogonality of sensor axes or misalignment between the gyro sensing axes and body coordinate system [Aggarwal \(2010\)](#).

$$M_G = \begin{bmatrix} 0 & m_{xy} & m_{xz} \\ m_{yx} & 0 & m_{yz} \\ m_{zx} & M_{zy} & 0 \end{bmatrix} \quad (2.38)$$

From [Niu et al. \(2013\)](#) it can be seen that surprisingly misalignment errors may also change with temperature for a particular gyroscope. It is here 0.6% over the range $-10 - 70^\circ C$ before calibration and 0.13% after.

2.5.3 Bias(B_g)

Bias Run-to-Run This is initial bias that changes from power on to power on and remains constant during a run [Aggarwal \(2010\)](#), [Titterton and Weston \(2004\)](#), [Grewal and Andrews](#)

(2010). More precise descriptions of this problem has not been found, but the problem is to a degree measured/illustrated in "A new approach to better low-cost MEMS IMU performance using sensor arrays" [Martin et al. \(2013\)](#).

Zero Rate Instability: This is the stochastic variation of in-run bias over time. From "An introduction to inertial navigation" [Woodman \(2007\)](#) we have that it is caused by flicker noise present in electronic components. Flicker noise has a power spectral density following $1/f$ and is most often observed as a low frequency component. In higher frequencies it is overshadowed by white noise. This specific type of noise is present in most electronics and has a constant standard deviation. It can be approximated/modeled as a random walk process, this involves growth of the standard deviation proportional to the square root of time.

Another method often used and one that seems more accurate is the 1^{st} order Gauss-Markov(GM) process. Use and theory on the GM process to model bias is well described in "Improving the Inertial Navigation System (INS) Error Model for INS and INS/DGPS Applications" [Nassar \(2005\)](#). Here the theoretical definition of bias as a random constant with constant standard deviation is given. The first-order differential equation used to model sensor residual bias as a 1^{st} order Gauss-Markov process and its implementation method is illustrated. The similarity of having a constant standard deviation with respect to time and how the process tends to being a random constant bias for increasing order towards inf is also shown.

Zero rate over temperature and acceleration The exact dependence here is a big question. "Gyro Mechanical performance" [Weinberg \(2011\)](#) and "Fast Thermal Calibration of Low-Grade Inertial Sensors and Inertial Measurement Units" [Niu et al. \(2013\)](#) shows this relationship to be very nonlinear with hysteresis.

"Error Modeling and Characterization of Environmental Effects for Low Cost Inertial MEMS Units" [Yuksel et al. \(2010\)](#) test two types of single axis gyroscopes from Analog Devices.

For one of the gyros, temperature dependence was shown to be stable over 3 weeks with a small linear acceleration bias. Thermal dependence for the second gyro varies significantly over the test periods. While testing gravity/acceleration sensitivity, turn on self heating effects are shown to be present for the first most stable gyroscope. The effect is compensated with the thermal compensation function from the temperature characteristics. It should be mentioned that orientation of gyros is not always clearly stated in this article.

The shape of many of the temperature responses shown in plots for the second gyroscope is very similar to what was shown in "Integrated Model and Compensation of Thermal Errors of Silicon Micro-electromechanical Gyroscope" [Jiancheng and Jianli \(2009\)](#). In this article the thermal effects are modeled and compensated as one part dynamically induced by acceleration, and one part static.

$$B_S = (k_{b1}\Delta T + k_{b2}\Delta T^2) + \epsilon_b \quad (2.39)$$

$$B_D = (k_{f_x}f_x + k_{f_z}f_z)\Delta T + (k_{\dot{\omega}_x}\dot{\omega}_x + k_{\dot{\omega}_y}\dot{\omega}_y + k_{\dot{\omega}_z}\dot{\omega}_z)\Delta T \quad (2.40)$$

The change in rate($\dot{\omega}$) thermal error was not verified. The type of gyroscope used in this article is a dual gimballed (DG) gyro, stated as possessing universal thermal error characteristics for MEMS rate sensors but it is not explicitly stated who made the gyroscope.

One method that can be used to correct for temperature effects demonstrated in "Error Modeling and Characterization of Environmental Effects for Low Cost Inertial MEMS Units" [Yuksel et al. \(2010\)](#) is mounting an array of gyroscopes with sensing axes in opposite directions and average the measurement. The result is described in the equation below taken from [Yuksel et al. \(2010\)](#)

$$\omega_z^{com} = 0.5(\omega^A - \omega^B) \quad (2.41)$$

$$= 0.5(\omega_z + c_1 t + c_2 a_x + c_3 a_y + c_4 a_z + \eta_a) \quad (2.42)$$

$$- 0.5(-\omega_z + c_1 t + c_2 a_x - c_3 a_y - c_4 a_z + \eta_b) \quad (2.43)$$

$$= \omega_z + c_2 a_y + c_4 a_z + 0.5(\eta_a - \eta_b) \quad (2.44)$$

2.5.4 Thermo Mechanical White Noise(ϵ_G)

Is very often described with power spectral density(PSD ($^\circ/s$)²/Hz), a root mean square(RMS) $^\circ/s$ for a certain bandwidth(BW) or the parameter angular random walk(ARW) $^\circ/h$ attained by plotting the Allan Variance of the gyroscope.

$$ARW = \frac{1}{60} \sqrt{PSD \left(\left(\frac{^\circ}{hr} \right)^2 / Hz \right)} \quad (2.45)$$

$$RMS = \sqrt{PSD \left(\left(\frac{^\circ}{hr} \right)^2 / Hz \right) * \sqrt{BW}} \quad (2.46)$$

These conversions are given straight up in [Stockwell \(2003\)](#) while Allan Variance is explained in [El-Sheimy et al. \(2008\)](#). A important point to notice from the conversions above is that ARW is not reduced with a lower bandwidth.

Chapter 3

Chosing Sensors

3.1 Finding And Evaluating Gyroscope Alternatives

3.1.1 Reading data sheets

It was somewhat a challenge to interpret gyroscope data sheets precisely because of a lack off referencing to standards and inn house descriptions of the presented parameters. In addition most of the manufacturers unfortunately give specifications in only a similar fashion, creating some uncertainty around how to compare and interpret numbers. There are plenty of specification standards available but the most appropriate for this purpose seems to be IEEE standard [IEE \(2014\)](#) and is therefor summarized shortly bellow. The standard introduction state the non-uniformity of data sheets as one of the reasons for making the standard.

For all commercial gyroscope datasheets seen, values are given as Max, Min or Typical and the IEEE standard [IEE \(2014\)](#) state "Max"/"Min" to be ± 3 standard deviation and the "Typical"

values to be a mean value or one standard deviation. All parameters should be true for specified operating voltage at room temperature(25°C) unless something else is mentioned.

Sensitivity gain or scale factor should be given as dps/LSB after PCB assembly, mechanical shock and over expected life time with ± 3 times standard deviation to indicate linear scale error.

Sensitivity temperature coefficient should be given as $\%/C$ of rotation rate, or for example $\pm\%$ for the entire temperature range. It is suggested that ramps are to be used when the relation is dominantly linear, whereas for non-linear relations \pm max expected values should be used. Discontinuities or jumps in the response should also be indicated.

Integral non-linearity or just non-linearity is a maximum deviation of measured output from the best fit straight line as a % of the full scale range(FSR).

Missalignment error is termed cross axis sensitivity/coupling error or skew and is a percentage of rate from two axes seen in the remaining axis.

Zero rate bias is explained as "Zero rotation rate output deviation from expected zero rotation rate output value for each sensing axis". This value should be correct over the lifetime of the component and after PCB assembly and mechanical shock.

Zero rate bias temperature coefficient should be given as a deviation from expected zero rate output because of changes in temperature from 25°C. Dominant behavior in terms of linear/non-linear response should be indicated using for example a ramp($(^{\circ}/s)/^{\circ}C$) for a linear relation while $\pm(^{\circ}/s)$ should be used for nonlinear. Discontinuities or jumps should also be indicated.

Linear acceleration sensitivity is found for the effect along any of the gyroscope axis and will in most gyroscopes appear as an alias of rotation rate in that axis.

White noise Can be represented in data sheets as rms($^{\circ}/s$) noise for a particular bandwidth and should be calculated as standard deviation for a minimum of 10 000 sample points. Noise density($^{\circ}/s/\sqrt{Hz}$) is also commonly given together with rms.

Angular Random Walk is a parameter that can be calculated from noise density, se eq 2.45. But it should be measured by plotting the Allan Variance of the gyroscope, per IEEE Std 647TM – 2006.

Zero rate instability is another Root Allan variance parameter describing the random variation in bias for finite time intervals of sampling and averaging. The parameter comes as $^{\circ}/h$ or $^{\circ}/s$ and is extracted from the same plot angular random walk is found.

3.1.2 Evaluating Alternatives

Firstly the alternatives presented in figures 3.1 and 3.2 were found by first determining the major manufacturers using Digikey, Mouser and Farnell. The manufacturer home pages were used to get an overview of all the digital alternatives of three axis gyroscopes. Those standing out with good rate noise density and/or bias temperature coefficient and a good temperature sensor were included in the alternatives presented here.

A good temperature sensor and bias stability over temperature is focused on because it is well known that the satellite will experience large temperature variations between an illuminated and shadowed state as exemplified in section 2.2. And the information found in literature on gyroscope errors presented in section 2.5 suggests that this error can be modeled to a lesser or higher degree of accuracy depending on the gyroscope.

Unfortunately the only information available on how good the gyroscope needs to be are simulations performed by Westgård (2015) testing the robustness of the controller with respect to noise on the rotation rate input. The simulations gave that the largest rate noise density the controller could handle was $0.0002[\text{deg}/\text{s}/\sqrt{\text{Hz}}]$.

Firstly the alternatives from Murata and Seikon Epson are quartz gyroscopes. The alternative from Murata was originally found just as an example because quartz gyroscopes are known to be more stable under temperature changes compared to the silicon based gyroscopes. Later the Seikon Epson alternatives were found and included because they are unquestionably the best alternatives seen to date in terms of rate noise density and bias stability over temperature. Unfortunately M-V34OPD has a much larger current consumption than any of the silicon alternatives (not from Murata or Seiko Epson) and the data sheet for XV7011BB says nothing about a temperature sensor. And the price for these gyroscopes is likely to be high because they are not available off the shelf. Therefore they are here considered an alternative only if pointing can not be made to work with one of the silicon gyroscopes.

Property	Manufacturer	INVENSENSE			STMICROELECTRONICS	
Name		MPU-3300	ICM-20608-G	ITG-3050	L3GD20H	I3G4250D
Sensing Axes		xyz	xyz	xyz	xyz	xyz
Range	[°/s]					
		±225	± 250	± 250	±245	±250
		±450	± 500	± 500	±500	±500
			± 1000	± 1000		
			± 2000	± 2000	±2000	±2000
Scale Factor/Sensitivity						
	[LSB/°/s (°/s/LSB)]					
		145.6 (0.00686)				
		72.8 (0.00137)	131 (0.00763)	131 (0.00763)	114.3 (0.00875)	114.3 (0.00875)
			65.5 (0.01526)	65.5 (0.01526)	57.1 (0.01750)	57.1 (0.01750)
			32.8 (0.03048)	32.8 (0.03048)		
			16.4 (0.06097)	16.4 (0.06097)	14.3 (0.07000)	14.3 (0.07000)
Scale Factor Nonlinearity	[%]	-	±0.1	±0.2	±0.2	±0.2
Scale Factor over Temperature		±2	±3	±2	±2	±2
	[%/(%T)]					
Scale Factor Error	[%]	-3 - +3	±2	-6 ±2 +6	-	-
Cross-Axis Sensitivity	[%]	±2	±2	±2	-	-
Acceleration Sensitivity	[°/s/g]	Static 0.1	-	Static 0.1	-	-
Bias Level	[°/s]	±20	±5	±20		±10
					±25	±75
Bias over Temperature		±20 (±0.25)*	±6.5* (±0.1)	±2* (±0.03)		±1.95* (±0.03)
	[°/s (°/s/dT)]					
					±2.6* (±0.04)	±2.6* (±0.04)
Bias Instability	[°/hr]	15	-	-	-	-
Rate Noise Density	[°/s/√Hz]	0.005	0.008	0.01	0.011	0.03
Angular Random Walk	[°/√hr]	-	-	-	-	-
Operating Temperature range		-40 to +105	-40 to +85	-40 to +105	-40 to +85	-40 to +85
	[°C]					
Temperature Scale Factor		0.00294	-	0.00357	-1	-1
	[°C or K/LSB]					
Current Drain	[mA]	3.6	2.9	5.9	5	6.1

Figure 3.1: List of most viable gyroscopes from each of the manufacturers. Values marked by a '*' are calculated from the values not marked to allow for a comparison. The values are taken from the data sheets

Property	Manufacturer	BOSH SENSORTECH	NPX	MURATA ELECTRONICS	SEIKON EPSON		
Name		BMG160	BMG250/280 (Preliminary)	FXA21002C	SCR1100-D02	XV7011BB	M-V340PD
Sensing Axes		xyz	xyz	xyz	x	z	xyz
Range	[°/s]	± 125 ± 250 ± 500 ± 1000 ± 2000	± 125 ± 250 ± 500 ± 1000 ± 2000	±250 ±500 ±1000 ±2000	±100	±100	±450
Scale Factor/Sensitivity	[LSB/°/s (°/s/LSB)]	262.4 (0.00381) 131 (0.00763) 65.5 (0.01526) 32.8 (0.03048) 16.4 (0.06097)	262.4 (0.00381) 131 (0.00763) 65.5 (0.01526) 32.8 (0.03048) 16.4 (0.06097)	128 (0.0078) 64 (0.0156) 32 (0.0312) 16 (0.0625)	50 (0.02)	280 (0.0035)	66 (0.015)
Scale Factor Nonlinearity	[%]	±0.05	-	±0.5	-	±0.5	±0.1
Scale Factor over Temperature	[%(°/T)]	±1.95*(±0.03)	-	±5.2*(±0.08)	-1 - 1 (±0.012)*	-	0.0010
Scale Factor Error	[%]	-	-	-	-2.0 - 2.0	±5	0.5
Cross-Axis Sensitivity	[%]	±1	-	±1.5	- - 1.7	±5	0.1
Acceleration Sensitivity	[°/s/g]	0.1	-	-	-0.1 - 0.1	-	0.01
Bias Level	[°/s]	±1	±3	±0.4	-1.0 - 1.0	±1	-
Bias over Temperature	[°/s (°/s/dT)]	±0.975* (0.015)	±3.25* (0.05)	±1.3* (±0.02)	-0.6 - 0.6 (±0.006)*	±1 (±0.015)*	±0.065* (0.001)
Bias Instability	[°/hr]	-	-	-	0.1	-	3.5
Rate Noise Density	[°/s/√Hz]	0.014	0.007	0.025	0.0085	0.003	0.0025
Angular Random Walk	[°/√hr]	-	-	-	0.45	-	0.17
Operating Temperature range	[°C]	-40 to +85	-40 to +85	-40 to +85	-40 to +125	-40 to +85	-40 to +85
Temperature Scale Factor	[°C or K/LSB]	0.5	-	1.0	-	-	-0.0053964
Current Drain	[mA]	5	5	2.7	24	0.9	18

Figure 3.2: List of most viable gyroscopes from each of the manufacturers. Values marked by a '*' are calculated from the values not marked to allow for a comparison. The values are taken from data sheets

Three gyroscopes stand out. The first is the MPU-3300 with the smallest noise rate density of $0.005[\text{deg}/s/\sqrt{\text{Hz}}]$ a temperature sensor with high resolution and unfortunately the absolutely highest bias over temperature change of $\pm 0.25 \text{ deg}/s/dT$. The second is BMG160 with the most stable bias over temperature of $0.015[\text{deg}/s/dT]$ but unfortunately with the highest rate noise density of $0.014 \text{ deg}/s/\sqrt{\text{Hz}}$. The third alternative to stand out is not a standalone gyroscope but the IMU160 with gyroscope rate noise density and bias stability equal to BMG250/280 of $0.007[\text{deg}/s/\sqrt{\text{Hz}}]$ and $0.05[\text{deg}/s/dT]$ respectively and a temperature sensor with a resolution of $0.002K/LSB$.

Not knowing anything about how repeatable the temperature characteristics of these gyroscopes are or how linear they are it is impossible to state that any one of these gyroscopes are best because ultimately it is the gyroscope that can be calibrated/compensated to the best results that will be most useful to the satellite. It is therefor recommended here to buy the MPU-3300, IMU160 and BMG160 and see witch one of them can give sufficiently good results together with calibration/compensation of temperature varying bias and a attitude estimation algorithm. All three gyroscopes is a improvement either in terms of noise rate density and or zero rate bias over temperature compared to the gyroscope L3G4200D currently installed on the ADCS. The data sheet of the L3G4200D is nearly identical to the I3G4200D. A interesting but slightly unfortunate trend visible for the gyroscopes presented here is that noise rate density seems increase when the bias over temperature is smaller on a gyroscope.

3.2 Sun Sensor Design

In this chapter the pyramid Sun sensor is first argued for as the best alternative for NUTS CubeSat. Following this a equation for finding photocurrent using data sheet values and spectral irradiance is suggested before a photodiode alternatives are discussed. Finally six very simple configurations of photodiodes is suggested and illustrate.

3.2.1 Sun Sensor Choise

Sun vector measurement accuracy less than 1 deg is not currently a goal for the nuts cubesat. With pyramid sunsensors requiering less parts than any other alternative found and presented in section 2.4. It should be the least power intensive and most importantly the most reliable solution. This is directly related to the low number of parts needed and to the fact that loss of one opamp/photodiode will not necessarily make others with intersecting FOW useless. Also this is the method originally implemented on the prototypes. Thus chosing this method will keep work needed to complete the solution to a minimum.

3.2.2 Photocurrent Equations

Finding an explicitly stated equation for photo/shortcircuit current for the parameters and effects summarized in section 2.4 was not possible. Therefor a theoretical photo current output is given bellow.

$$I_p(\theta_z, K) = S_A(\theta_z)C_T(K)A \int R(\lambda)E(\lambda) d\lambda \quad (3.1)$$

$$I_{\theta_0}(K) = I_p(0, K) \quad (3.2)$$

This equation is a logical outcome of the photodiode parameters as given in section 2.4. The only parameter not named previously is A that is area of sensitive surface. From [Bhanderi and Bak \(2005\)](#) we have that a conversion factor K_R from incoming irradiance to current can be found experimentally following.

$$K_R = \frac{I_{\theta_0}}{E_{\theta_0}} \quad (3.3)$$

Where E_{θ_0} is a known irradiance normally onto the photodiode giving measured current I_{θ_0} . Using equation 3.1 and those given in section 2.4 on PIN photodiodes the full theoretical expression for such a constant should be.

$$I_{\theta_0} = C_T(K) R_{\lambda_{max}} A \int S_R(\lambda) E(\lambda) d\lambda \quad (3.4)$$

$$I_{\theta_0} = C_T(K) R_{\lambda_{max}} A E_{\theta_0} \quad (3.5)$$

$$K_R(K) = C_T(K) R_{\lambda_{max}} A \quad (3.6)$$

$$K_R(K) = \frac{E_{\theta_0}}{I_{\theta_0}} \quad (3.7)$$

$K_R(K)$ as found here is clearly completely independent of relative spectral sensitivity but correct irradiance actually being converted to current E_{θ_0} is needed. This is her termed effective irradiance. The conversion factor can also be found and corrected using the Sun as input while the satellite is in space as done in [Springmann and Cutler \(2014\)](#) and [Ortega et al. \(2010\)](#).

3.2.3 Chosing A PIN Photodiode

Because Earth albedo is a significant problem when measuring the Sun direction. Considering the spectra of reflected light from Earth presented in section 2.3.3. It seems there is an advantage in looking for photodiodes with responsivity in the H^2O absorption bands around $900nm$, $1100nm$ or $1400nm$. Also to keep output changes with respect to temperature minimal, high shunt resistance and a low temperature coefficient is desirable. Lastly a angular response as close to a cosine curve as possible is high on the priority list.

InGaAs Solution

First for the most interesting absorption band where practically no irradiance from Earth is present (approximately $1350 - 1450nm$), a possible solution was found. InGaAs PIN photodiodes have sensitivity in the area $1000nm$ to somewhere above $1600nm$. They are preferred in many applications for a relatively high shunt resistance (around $10M\Omega$) for near infrared sensors. They have good thermal stability in the relevant range, $1350 - 1450nm$. Examples of these properties can be found on available sensors from "Hamamatsu" [Ham](#). And relatively sharp band pass filters for precisely this range is available, from for example "Optical Filter Shop" [Opt](#).

The disadvantages of going for such a solution is firstly that it is untried for the less experienced level of student CubeSats known to this author. A quick Google image search will make the H^2O absorption bands fairly obvious. Therefore it is strange such a solution to Earth albedo dose not stand out in literature. This makes it likely that obstacles are present, not immediately obvious. And consequently there are large uncertainties for questions such as. How are filters built and how robust they are to conditions such as vacuum and temperature cycling? Will Filtering characteristics depend on the direction light is incident on the filter? And how will the angular response be after the filter? It is also believed that mounting these two components together will involve significant challenges.

Because of the risk these unknowns present the InGaAs solution is dropped in this thesis where reliability of Sun direction measurement and ease of implementation is a concern before novelty. Thought as experimental payload this is interesting if further research is done.

Silicon PIN Photodiodes

Silicon PIN Photodiodes have sensitivity in the approximate range from $200nm$ to $1100nm$ and they usually have a very high shunt resistance from $10M\Omega$ s to $1000M\Omega$ s [OSI](#). Also as previously mentioned in section [2.4](#) silicon PIN photodiode SFH2430 from OSRAM was used successfully on RAX *I* and *II* and is still available to buy and will be investigated further as an alternative.

Using Farnel, Mouser and Digikey a search for PIN photodiodes with spectral responses around $900nm$ and angle of half sensitivity at $60deg$ was performed. From the remaining alternatives a visual search for cosine curves narrowed down options further. Unfortunately many producers don't give plots of angular sensitivities on data sheets and are thus excluded. Under these conditions the best remaining alternatives are from Vishay and OSRAM.

From OSRAM we have BPW34FAS, BPW34FS and SFH2430 as the best alternatives. While all the flat packaged photodiodes from OSRAM have angular sensitivity following a perfect cosine response on data sheets only the BPV22-23F series and VEMD6110X01 from Vishay come close to this. BPV22-23 stands out with a visibly narrower spectral bandpass compared to those from OSRAM and is therefore also included in the evaluation. The angular sensitivity of alternatives can be seen in figure [3.3](#) together with the ideal case in red and with approximated reflection in blue as given in section [2.4](#). The spectral sensitivity is given in figure [3.4](#) together with Earth reflectance extracted from figure 7.7 in [Gottwald and Bovensmann \(2010\)](#) using the plot digitizer [Rohatgi \(2011\)](#). The sensitivity is also given in figure [3.5](#) together with Sun and Earth irradiance. The Earth irradiances were found using extracted data plotted in figure [3.4](#) and plotted Sun

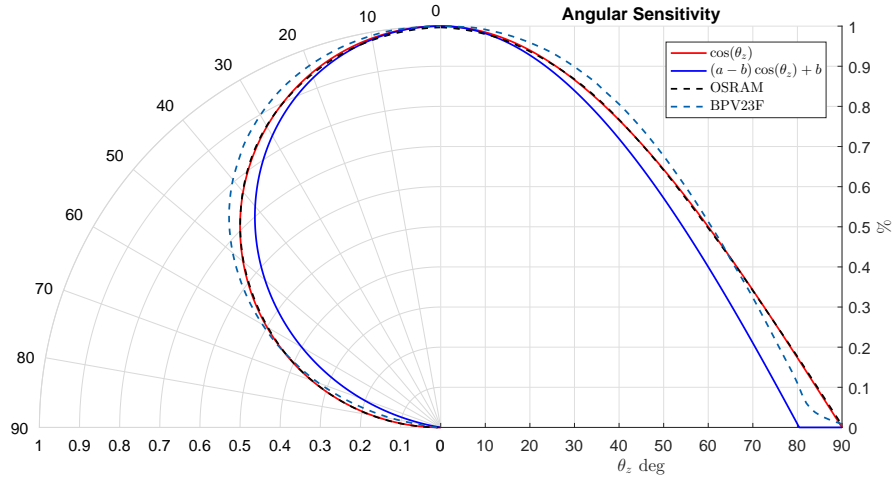


Figure 3.3: Red curve represents ideal lambertian(cosine) angular response. Blue is the non ideal case with the effect of reflection approximated as in equation 2.32 with $a = 1, b = -0.2$. For OSRAM photodiodes angular sensitivity of BPW 34 FAS, BPW 34 FS and SFH2430 is identical and recreated here in black lines together with BPV23F using a plot digitizer Rohatgi (2011)

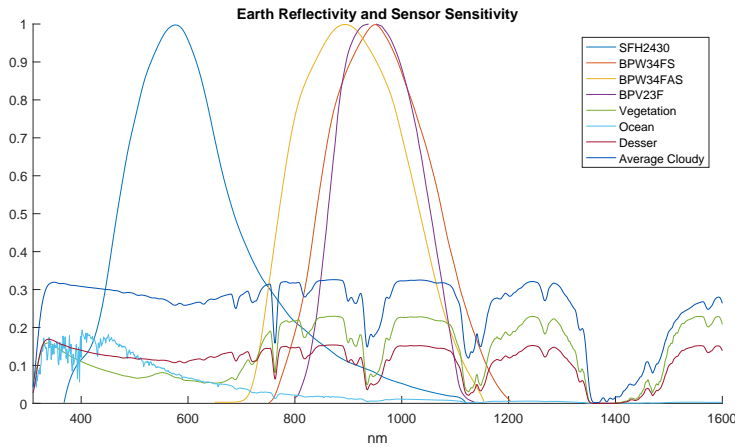


Figure 3.4: Relative spectral sensitivity for OSRAM photodiodes BPW 34 FAS, BPW 34 FS, SFH2430 and Vishay BPV23F recreated here using the plot digitizer Rohatgi (2011). Together with Earth reflectance extracted from figure 7.7 in Gottwald and Bovensmann (2010) using the graph digitizer Rohatgi (2011)

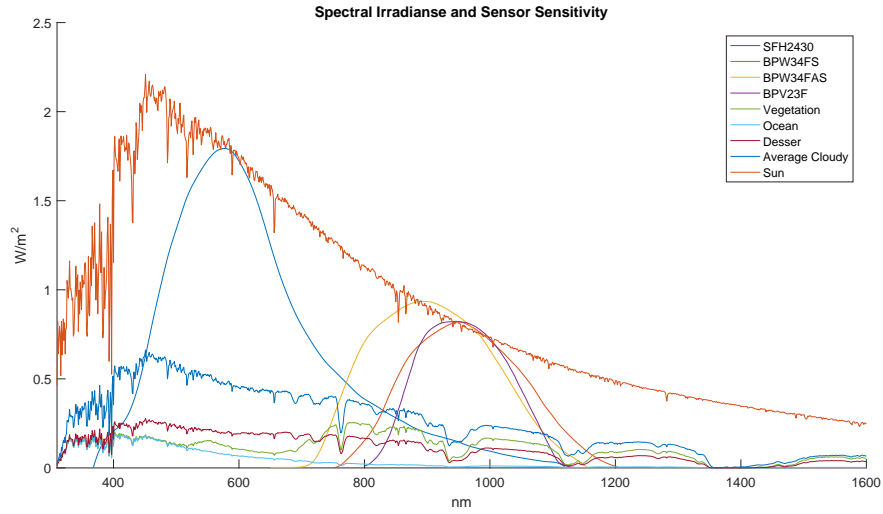


Figure 3.5: Relative Spectral sensitivity from datasheets for photodiodes from OSRAM, BPW 34 FAS, BPW 34 FS, SFH2430 and Vishay BPV23F recreated here using the graph digitizer Rohatgi (2011). They are scaled to Sun irradiance at peak sensitivity for illustration purposes here and are normally a percentage of irradiance converted to current. Sun irradiance is the same as given in figure 2.1. Earth irradiances are created using plotted Sun spectra and reflectance extracted from figure 7.7 in Gottwald and Bovensmann (2010) using Rohatgi (2011)

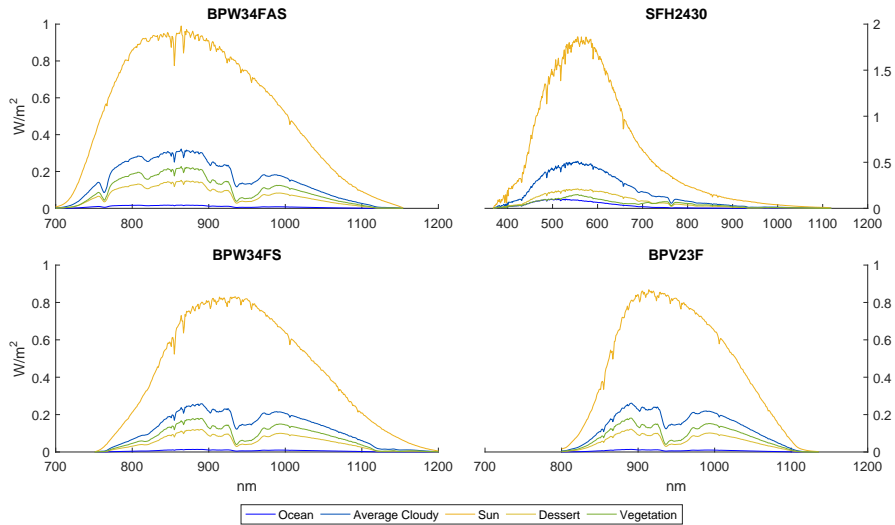


Figure 3.6: $E_{\theta_0}(\lambda) = S_R(\lambda)E(\lambda)$ for OSRAM photodiodes BPW 34 FAS, BPW 34 FS, SFH2430 and Vishay BPV23F made using irradiance values illustrated in figure 3.5 and relative sensitivities as illustrated in 3.4. Where $E(\lambda)$ are irradiance values and $S_R(\lambda)$ is the relative sensitivity of the specified photodiodes.

irradiance. The data in figure 3.5 will be used to see if any of these photodiodes experiences a smaller value of Earth reflection.

For the data plotted in figure 3.5, $E_{\theta_0}(\lambda) = S_R(\lambda)E(\lambda)$ is calculated and plotted in figure 3.6 for each of the photodiodes. Summing up $S_R(\lambda)E(\lambda)$ using the trapezoid method we get effective irradiance for each of the sources and photodiodes. Resulting value from the Sun is given in table 3.2.3 under the notation $E_{S\theta_0}$. For the different photodiodes, the reflected irradiance values have been normalized with respective $E_{S\theta_0}$ to give Earth reflectance as experienced per photodiode.

	$E_{S\theta_0} [W/m^2]$	Average Cloudy	Vegetation	Dessert	Ocean
SFH2430	425.9	0.2789	0.0838	0.1194	0.0463
BPW34FS	188.1	0.2836	0.1809	0.1215	0.0138
BPW34FAS	234.3	0.2894	0.1855	0.1265	0.0154
BPV23F	154.1	0.2822	0.1793	0.1203	0.0135

Unfortunately the reduction of Earth reflectance as experienced by photodiodes versus the expected average of 30% is small for all the alternatives that has been found and presented here. Clearly a much narrower band of sensitivity is needed to get more significant improvement with respect to Earth albedo. With BPV23F not being much better than alternatives from OSRAM that have better angular sensitivity, BPW34FS and surprisingly SFH2430 stand out.

SFH2430 will be much better for surfaces of vegetation and slightly worse for oceans. On average with clouds it is a tiny bit better than BPW34FS. With the differences between these two being so small with respect to measured albedo it can not be used as a major argument for or against one of them.

SFH2430 has the major advantage of flight history. We know that it works in space with degradation of responsiveness if it is not shielded as on RAX II [Springmann and Cutler \(2014\)](#). BPW34FS has the same type of packaging as SFH2430 but with daylight filtering black epoxy instead of the

clear epoxy. With the producer and packaging being identical for the two it is intuitive that the risk of BPW34FS failing due to unforeseen circumstances should not be much different compared to SFH2430.

The main advantage BPW34FS has over SFH2430 is a much smaller temperature coefficient, $0.03\%/K$ versus $0.16\%/K$ and much higher peak responsivity $R_{\lambda_{max}}$, $0.7A/W$ versus 0.17 . The increased responsivity should make BPW34F provide a higher current output versus noise induced in wiring to the operational amplifiers. For these two reason BPW34FS can be recommended her for the possibility of slightly higher performance while SFH2430 is a more predictable/safer alternative.

3.2.4 Mounting Orientation

The prototype of the Sun sensor consisted of 6 photodiodes mounted on the six sides of the cube satellite, a quick upppgrade to 12 in the same orientations gives redundancy. The goal of this section is to illustrate other alternatives of photodiode mounting that preserves or improves the redundancy while also allowing for reduced field of view(FOV). With the current hardware setup there is room for a total of 16 photodiodes. For these we will here create sets of photodiode orientations that will later be tested in a simulation to see how they perform.

With the RAX Cube Satellites and the PhD thesis [Springmann \(2013\)](#) as inspiration a couple of visual aids where made to illustrate how many photodiodes are able to see a pixel of the attitude sphere. The very convenient MEALPIX library for Matlab® based on [Gorski et al. \(2005\)](#) was used to divide the attitude sphere into center pixels of equally sized patches/surfaces. For each patch a color is assigned representing either 2 and less(red), 3(yellow) and 4 or more(green) photodiodes, having that area center within its field of view(FOV). This is plotted in a spherical coordinate system of the satellite body frame. The idea behind the configurations presented

here is that side panels will have more room for mounting of sensors. The orientations of photodiodes found in [Springmann \(2013\)](#) is the inspiration for the configurations presented here but with redundancy as focus and the assumption that mounting will not be performed amazingly precisely. The original alternative with assumed 90 deg FOV on each sensor can be seen plotted in figure 3.7. The field of view(FOV) angle as talked about in this thesis is the largest angle away from photodiode normal that a vector of light is measurable.

Photodiode Configuration Tilt 00 FOV 90

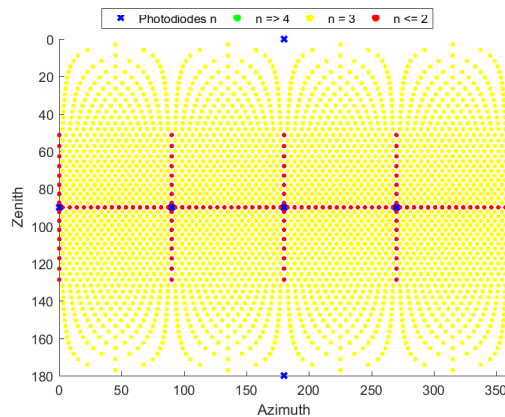


Figure 3.7: 6 sensors mounted on each side of the satellite with normals along satellite panel normals. Each dot represents a area of equal size on a sphere

Any angular characteristic given on data sheets are of course statistical average values. The lines of red dots is a result of reducing the acceptance to a tiny bit less than given FOV to represent this uncertainty. Following figures [3.9](#), [3.8](#), [3.11](#), [3.10](#) [3.13](#) and [3.12](#), illustrate configurations of photodiodes tilted/angled 20 deg, 25 deg and 30 deg away from side panels in both azimuth and zenith. For each of these cases 14 photo diodes are used and the field of view is reduced with 15 deg and 20 deg. In all cases one photodiode is set as dead.

The two last photodiodes should be mounted flatly on top and bottom panels together with those already there, making lost redundant area(yellow) less if one of these should be lost. It should be clear that two such photodiodes only give redundancy for those already mounted in equal direction.

Photodiode Configuration Tilt 20 FOV 75

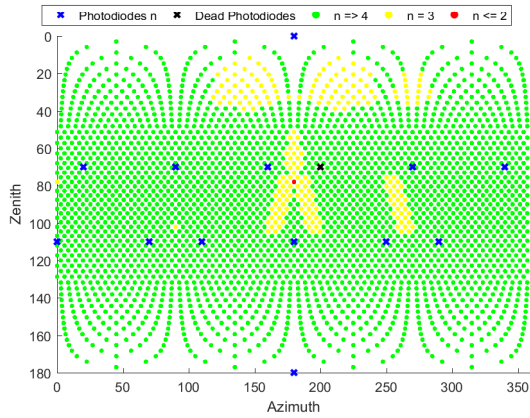


Figure 3.8: Red: 0.0003%. Yellow: 0.0667%. Green: 0.9329%. Photodiodes field of view reduced with 15 deg. Photodiode normal oriented 20 deg away from mounting surface normals in both azimuth and zenith

Photodiode Configuration Tilt 20 FOV 70

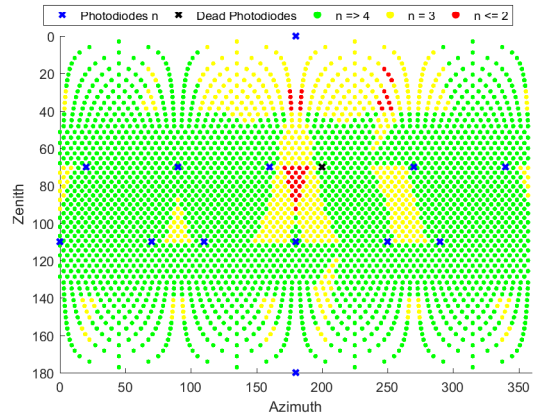


Figure 3.9: Red: 0.0117%. Yellow: 0.1751%. Green: 0.8132%. Photodiodes field of view reduced with 20 deg. Photodiode normal oriented 20 deg away from mounting surface normals in both azimuth and zenith

Photodiode Configuration Tilt 25 FOV 75

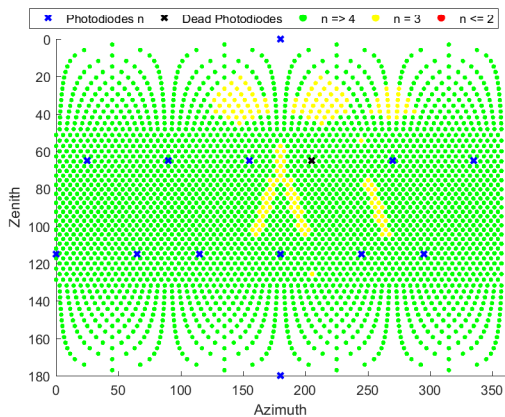


Figure 3.10: Red: 0.0000. Yellow: 0.0521. Green: 0.9479. Photodiodes field of view reduced with 15 deg. Photodiode normal oriented 25 deg away from mounting surface normals in both azimuth and zenith

Photodiode Configuration Tilt 25 FOV 70

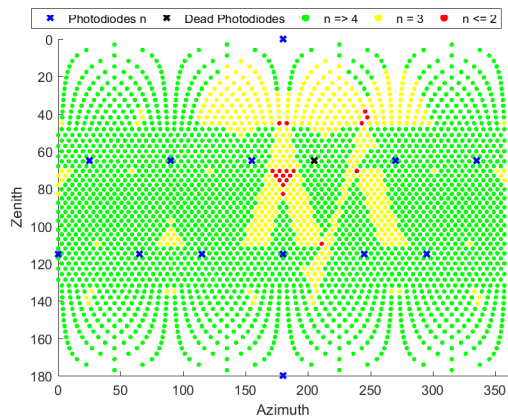


Figure 3.11: Red: 0.0059. Yellow: 0.1579. Green: 0.8363. Photodiodes field of view reduced with 20 deg. Photodiode normal oriented 25 deg away from mounting surface normals in both azimuth and zenith

Photodiode Configuration Tilt 30 FOV 75

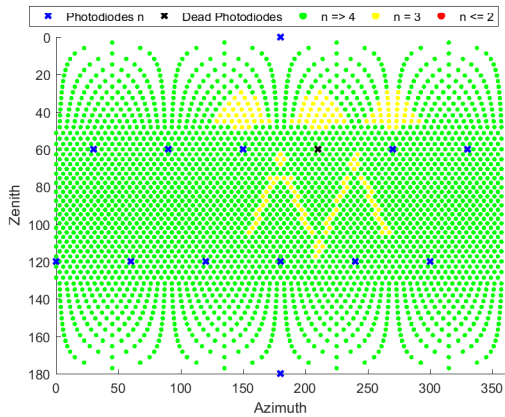


Figure 3.12: Red: 0.0000. Yellow: 0.0508. Green: 0.9492. Photodiodes field of view reduced with 15deg in all directions. Photodiode normal oriented 30deg away from mounting surface normals in both azimuth and zenith

Photodiode Configuration Tilt 30 FOV 70

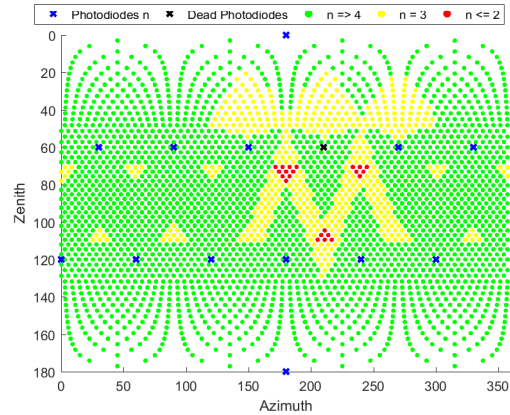


Figure 3.13: Red: 0.0072. Yellow: 0.1514. Green: 0.8415. Photodiodes field of view reduced with 20deg. Photodiode normal oriented 30deg away from mounting surface normals in both azimuth and zenith

The different photodiode orientations dose not change the amount of green area to any significant degree. Clearly and not surprisingly, limiting photo diode view with only 15deg is advantageous for redundancy. Overall it can also be seen that spreading the photodiodes out more evenly gives smaller regions of lost redundancy(yellow). These configuration will be simulated in the next section to see which ones are best for Sun vector estimation.

Chapter 4

Simulation of Sun Sensor output and Sun Vector Estimation

The different components needed to simulate Sun sensor measurements will be presented here. Resulting simulated sensor output will then be given and discussed before Sun vector estimation methods and results are given per method. Finally disadvantages and advantages of the methods are discussed. The entire simulation is done in Simulink® using Matlab® function blocks within the subsystems, Environmental Input, Satellite Hardware, and Software as shown in figure [4.1](#).

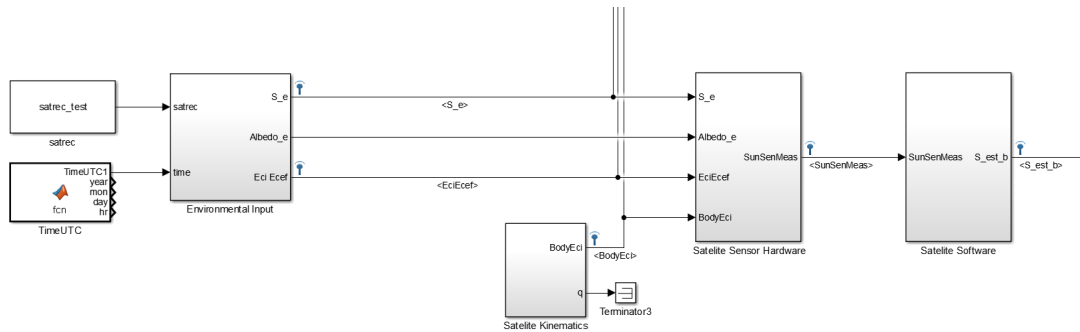


Figure 4.1: The complete Simulink® simulation of Sun sensor output and vector estimation illustrated with its subsystems.

4.1 Environmental Input Model

Consists of parts shown in figure 4.2. The SGP4 orbit Estimation model, Sun Vector model and ECI, ECEF frame rotations are matlab versions of C code implemented on the ADCS and made easily available for use by Pignede in his work [Pignede \(2015\)](#). In addition to these models the complete set of prediction algorithms used on the CubeSat also include two Geo Magnetic Field Models. Both the international geomagnetic reference field, IGRF and World Magnetic Model, WMM is available for use on the satellite and in Matlab, simplified for ease of use. Of the two the WMM is shown to be significantly faster and was therefor recommended. All models have been verified to work correctly against original code, similar alternatives and/or calculators available on the web [Pignede \(2015\)](#).

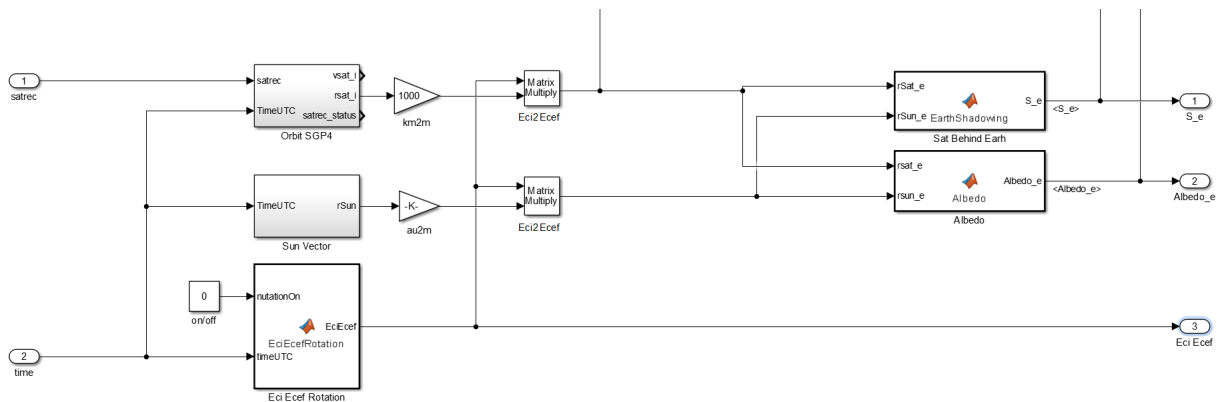


Figure 4.2: An overview of all Simulink® blocks in the environmental input subsystem.

The Albedo model is mostly code taken from the Matlab® library made by Bhanderi [Bhanderi \(2008\)](#). Implementation of the remaining algorithms shown in figure 4.2 and making the Matlab® code workable in Simulink was done by this author. Further details on all the algorithms will follow.

As can be seen in figure 4.1 the prediction algorithms depend on Universal Time Coordinated, UTC. This is also true for the magnetic field model used.

4.1.1 ECI,ECEF Frame Rotation

This function implements the frame rotation between ECI(Geocentric Equatorial Reference) and ECEF(International Terrestrial Reference) frame. The function takes into account the effect of precession, nutation, sidereal time displacement and polar motion using rotation matrices. Together they form a frame transform between ECI and ECEF that is only dependent on a UTC time input. The alternative to turn off further update of the nutation effect after the first simulation step was added by this author. The reason is that this calculation required a lot of time and the effect within the time scales simulated here was on the order 10^{-6} [deg], and therefore considered inconsequential in this simulation. The function executed is given below.

$$R_i^e = \text{EciEcefRotation}(\text{nutationOn}, \text{timeUTC}) \quad (4.1)$$

Nutation on is a simple boolean input used to allow on and off of this calculation which is always off in simulations shown in this thesis. TimeUTC is a struct containing the time and date used for the simulation. More details on this frame transform can be found in [Pigned \(2015\)](#)

4.1.2 SGP4 Orbit Model

The Orbit Position is estimated using the Simplified General Perturbations 4 model(SGP4). The model originates from "Spacetrack Report no. 3" and is popular because it is a good compromise between speed and precision [Pigned \(2015\)](#). The Matlab model used in this work gives a position vector in TEME frame transformed to the ECI frame in the order of kilometers. In addition to a struct containing time in the UTC format(*TimeUTC*) the function takes a struct named *Satrec* created at the start of simulation from a two-line element set with the function *OrbitTwoline2rv*. Two-line element set's describes an actual satellites orbit and can be acquired from the "CelesTrak" website [Kelso \(2015\)](#). for many satellites in orbit these will be available some time after launch. A small function was also made that structures a copy paste textfile from "CelesTrak" into the correct string format used by *OrbitTwoline2rv* and puts them all in a struct. The output from this function is rotated to ECEF and scaled to meters because this is what the Albedo function needs. The resulting output used by the Albedo function and Earth Shadowing is summarized in the equations under with functions and input.

$$\mathbf{r}_{b/i}^i = \text{OrbitSgp4}(\text{Satrec}, \text{TimeUTC})[\text{km}] \quad (4.2)$$

$$\mathbf{r}_{b/i}^e = \mathbf{R}_i^e \cdot \mathbf{r}_{b/i}^i \cdot 10^3 [\text{m}] \quad (4.3)$$

4.1.3 Sun Vector Model

The Sun vector algorithm used here gives a vector pointing from Earth to the Sun in ECI frame with length in astronomical units AU, it is normalized on satellite software and converted to meters using $1AU = 149597870700m$ in this simulation because of the Albedo function. And is also naturally rotated to the ECEF frame.

The inaccuracy of the model is not larger than 0.01 deg caused mainly by the approximation of Earth orbit parameters. The orbit of Earth around the Sun is what this model in reality describes. The matlab function is named *sun* and only needs *timeUTC*. The resulting vector gives the position of the Sun body frame with respect to ECI.

$$\mathbf{r}_{s/i}^i = \text{Sun}(\text{TimeUTC}) \quad (4.4)$$

$$\mathbf{r}_{s/i}^e = \mathbf{R}_i^e \cdot \mathbf{r}_{s/i}^i \cdot 149597870700[m] \quad (4.5)$$

For Sun position the letter *s* is used for a frame centered at the Sun, needed to properly follow the convention of frame notation for positions of physical objects.

4.1.4 Earth Shadowing

The Sun position vector is changed to Sun irradiance by including shadowing from Earth and rescaling the vector to Sun average constant of irradiance E_{ET} . The Earth shadowing function is a naive function because it does not take into account atmospheric effects or small orbit dependent changes to irradiance. It is based on geometry using satellite position, Earth mean radius and the Sun direction. The concept is illustrated in figure 4.3.

The critical angle when the satellite moves behind the Sun, θ_{crit} can be found as follows,

$$\theta_{crit} = \arccos\left(\frac{EMR}{\|\mathbf{r}_{b/i}^e\|}\right) \quad (4.6)$$

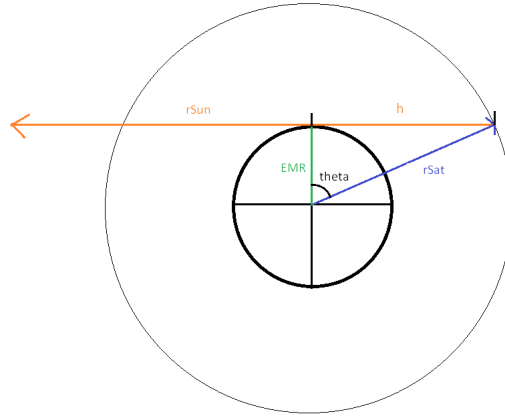


Figure 4.3: Geometry used to simulate Earth shadowing. θ is angle used to determine if the satellite is in shadow or not. "rSat" and "rSun" is satellite position and Sun position. h is the distance from Earth horizon to satellite position at θ_{crit} and EMR is Earth mean radius

using the norm of $\mathbf{r}_{b/i}^e$, Earth Mean Radius $EMR = 6371.01e3$ and the Sun direction $\mathbf{d}_{Sun} = \frac{\mathbf{r}_{s/i}^e}{\|\mathbf{r}_{s/i}^e\|}$. The angle θ is found using the relation shown in the equations under. Frame notation has been dropped to keep the notation cleaner.

$$h = -\mathbf{r}_b \cdot \mathbf{d}_{Sun} \quad (4.7)$$

$$h = \|\mathbf{r}_b\| \sin(\theta) \quad (4.8)$$

$$\theta = \arcsin\left(\frac{-\mathbf{r}_b \cdot \mathbf{d}_{Sun}}{\|\mathbf{r}_b\|}\right) \quad (4.9)$$

When θ is larger than θ_{crit} the Sun vector returned by the function is set to zeros, else it is given the length E_{et} . Expressed as a equation output from the function is as given under.

$$s = \begin{cases} E_{ET} \frac{\mathbf{r}_s}{\|\mathbf{r}_s\|}, & \text{if } \theta > \theta_{crit} \\ \mathbf{r}_{Sun} \cdot \mathbf{0}, & \text{else} \end{cases} \quad (4.10)$$

With input to this function being $\mathbf{r}_{b/i}^e$ and $\mathbf{r}_{s/i}^e$ the notation chosen for the vector of irradiance at the satellite body frame pointing to the source expressed in ECEF frame \mathbf{s}_b^e .

4.1.5 Albedo Model

The library provided by Bhanderi has a simulink block that executes the equations giving reflected irradiance presented in subsection 2.3.4, for each significant cell. The Albedo block is not used, instead the function within is used and cleaned up to a slimmer version without extra plotting functions. Also a parallel processing version of the function was made with Matlab *parfor* loops. Originally this was intended to speed up things before it was discovered that its only supported outside Simulink, where the effect is significant.

Output from the function `albedo_slim`, \mathbf{alb}^e is a matrix representing the full map of Earth where each index corresponds to a spherical coordinate in ECEF frame. This is the same format that was used for the reflection map that is termed *data* here. If a cell of Earth surface affects the satellite with irradiance the value of irradiance is in the \mathbf{alb}^e matrix at the index corresponding to that patch of Earth.

$$\mathbf{alb}^e = \text{albedo_slim}(\mathbf{r}_{b/i}^e, \mathbf{r}_{s/i}^e, \mathbf{data}) \quad (4.11)$$

To make the irradiance values useful they must be given a direction. Originally the library provided by Bhanderi used a function `ss_proj` that projected the irradiance onto a sensor normal. This function was slightly changed to output irradiance directions, corresponding irradiance from \mathbf{alb}^e and source positions in ECEF fram. These vectors pointing to the source of radiance from the satellite body frame expressed in ECEF frame are available in the matrix \mathbf{Albedo}_b^e together with irradiance values. This was done to separate environmental input from hardware simulation.

$$\mathbf{Albedo}_b^e = \text{CreateAlbedoVectors}(\mathbf{r}_{b/i}^e, \mathbf{alb}^e) \quad (4.12)$$

At this point it is also possible to simulate the satellite with incident light from the Sun and Earth. Such a simulation result is illustrated in 4.4.

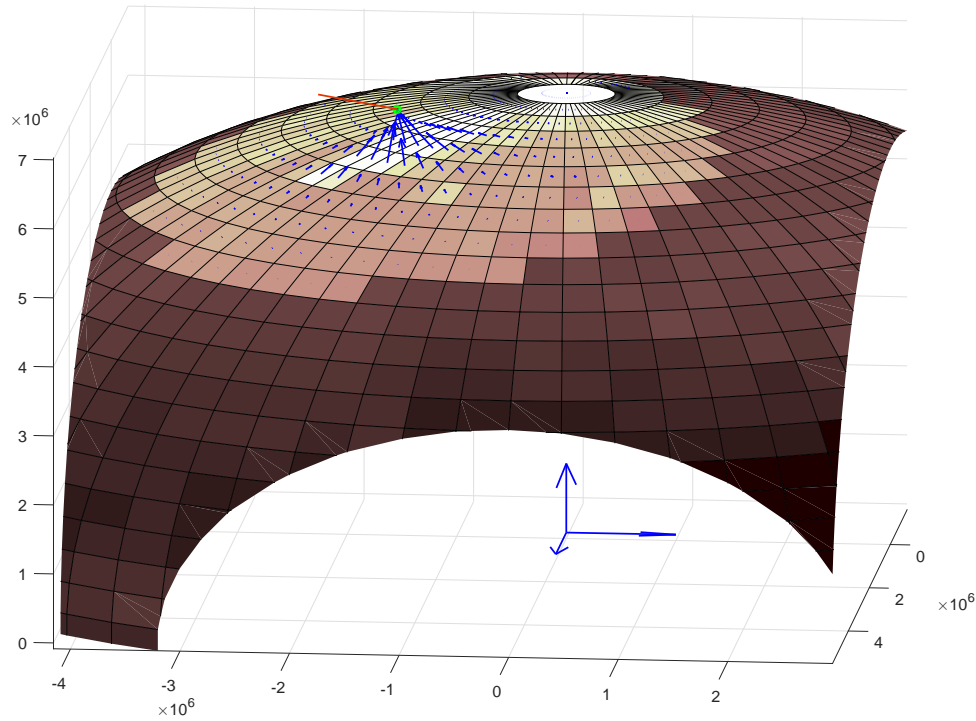


Figure 4.4: A illustration of the Sun vector in red, Earth reflected irradiance vectors in blue repositioned to sources with negative directions. All vectors are scaled up to make them visible. The green dot is the satellite, lighter colors on Earth represents higher reflectivity on the albedo map. This illustration is in the ECEF frame with coordinate system illustrated as the big blue arrows. The simulation here is under the same settings used in section 4.3 and at time $2.55 \cdot 10^4$ [sec]

4.2 Satellite Sensor Hardware

In this block s_b^e and the vectors of reflected light in \mathbf{Albedo}_b^e is mapped onto photodiode normals and rescaled to the irradiance converted to current by the photodiode. Details of this is described in the first subsection 4.2.1. The second subsection 4.2.2 talks about the operational amplifier used to convert photodiode current to voltage and simulation of the ADC.

4.2.1 Photodiode Output

Finding current output starts with the photodiode normals representing a mounting configuration as described in the previous section. These are for convenience defined to be in the satellite body frame $H_{b/i}^b$. All individual photodiode normals $\mathbf{n}_{pi\ b/i}^b$ is here rotated to the ECEF frame as follows.

$$\mathbf{n}_{pi\ b/i}^e = R_i^e R_b^i \mathbf{n}_{pi\ b/i}^b \quad (4.13)$$

The satellite body frame rotation is implemented with R_b^i using the MSS GNC Matlab® toolbox [Perez et al. \(2006\)](#). From here on the frame notation is dropped to keep the notation cleaner. For each of the albedo vectors and the Sun vector a cosine value is found for each of the photodiodes representing their cosine response C_{si} . The only difference between the calculation of the Sun measurement and albedo measurement is that there are several albedo vectors of irradiance onto the photodiodes. To shorten this section only the equations for the Sun input is given here. Once again frame notation is dropped to keep things cleaner.

$$C_{si} = \mathbf{n}_{pi}^T \mathbf{s} \quad (4.14)$$

After the FOV limit implemented by a physical aperture as talked about in section 3.2 and simply illustrated in figure 4.5. The angular response A_{si} will naturally change from C_{si} because less of the sensing surface is seen. To simulate this a approximated linear reduction in surface area with respect to angle of incident light is implemented as follows giving the final angular response used for the photodiode i .

$$A_{si} = \begin{cases} C_{si}, & \text{if } C_{si} \geq \cos(FOV) \\ C_{si} \frac{C_{si}-0.12}{\cos(FOV)-0.12}, & \text{if } \cos(FOV) > C_{si} \geq 0.12 \\ 0, & \text{if } C_{si} < 0.12 \end{cases} \quad (4.15)$$

Where $\arccos(0.12) = 83[deg]$ is the angle(with respect to sensing surface normal) where incident light no longer hits the sensing surface of the photodiode. This angle was chosen such that the total height of the entire aperture from the panel surface is only 6[mm] for 30[deg] tilt, FOV limited at $FOV = 70[deg]$ and photodiode BPW34FS. The expected launch pod for the NUTS CubeSat has a clearing of 9[mm] from the panel surface to pod interior.

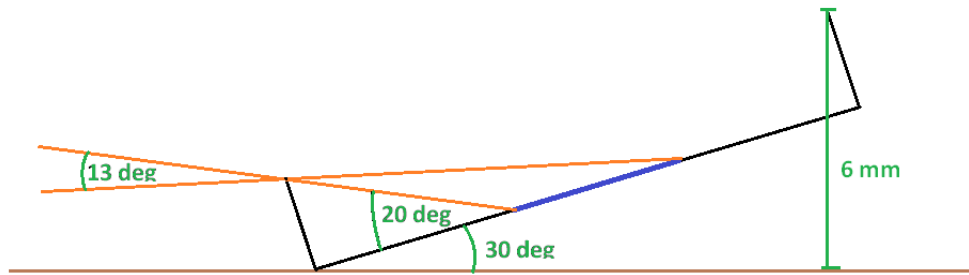


Figure 4.5: Blue line is photodiode sensing surface, orange lines represent Sun irradiance, black lines is the FOV limiting aperture and brown lines represents a satellite panel. This is a conceptual sketch illustrating how the FOV is limited.

Input from the Sun to sensors in this block is scaled down to effective irradiance for the photodiode BPW34FS, $E_{S\theta_0} = 188.1$. The reflected light is scaled down by the same amount.

$$I_{\theta_0} = K_{Ri} E_{S\theta_0} \quad (4.16)$$

$$I_{\theta_0} = S_A(0) R_{max} A E_{S\theta_0} \quad (4.17)$$

$$0.924[mA] = 0.7[A/W] * 7.02 * 10^{-6}[m^2] * 188.1[W/m^2] \quad (4.18)$$

The R_{max} value is often termed peak sensitivity in data sheets instead of responsiveness and is given for 25[deg/C]. Simulation of temperature changes and its effect on this photodiode has been dropped here because BPW34FS reacts so little to it. With this current for a photodiode in response to the Sun vector is

$$I_{pi} = I_{\theta_0} A_{si} \quad (4.19)$$

4.2.2 Operational Amplifier and ADC

The analog to digital converter on the UC3C can sample from $-1[V]$ to $1[V]$ and has preamplifier's of 1, 2, 4 and 8 times input and higher. Keeping the initial amplification at 1 would be advantageous because the first steps of not as high amplification may be used to keep loss of sensor resolution due to degradation. Leaving room for mistakes should also be done to avoid saturation therefor an amplification to around $0.5[V]$ should be most appropriate.

All simulation of satellite attitude control has been done with a step time of 1 second in the work done by Westgård [Westgård \(2015\)](#). In practice we have that our satellite will have a orbit time around 100 min for Sun synchronous orbit, corresponding to a nadir pointing rotation rate of $360/(100 * 60) = 0.06[\text{deg}/s]$. Our observed Sun vector is naturally going to with this rate in body frame and therefor have a frequency of $\frac{0.06[\text{deg}/s]}{360} = 0.000167[Hz]$. Testing a sine function of this frequency through the first order low pas filter

$$H_f(s) = \frac{3.0303}{s + 3.0303} \quad (4.20)$$

with bandwidth $0.5[Hz]$ gave a arcsine error of proximately $0.3[deg]$ between input and output of the filter, clearly there is no issue with the large step time. There are several ways to convert photo diode output from current to voltage and amplifying to a convenient value. From OSI optoelectronics application note [OSI](#) and several others it is stated that photovoltaic mode amplification has less variations in responsiveness with temperature. It is used in low light level conditions and is a relatively simple circuit. There was not time to gain a detailed understanding of how photovoltaic mode amplification works, therefor equations and information from application sheets are used directly. Conversion and amplification simply follows,

$$V_{pi} = I_{pi} \cdot R_F \quad (4.21)$$

for a transimpedans amplifier with a photodiode. For stability and reduction of bandwidth the capacitor C_F should be chosen using the following equations

$$\frac{1}{2\pi R_F C_F} < \sqrt{\frac{GBP}{2\pi R_F (C_J + C_F + C_A)}} \quad (4.22)$$

$$f_{op} = \frac{1}{2\pi R_F C_F} [Hz] \quad (4.23)$$

Where C_J is photodiode junction capacitance, C_A is amplifier input capacitance and f_{OP} is operating bandwidth. GBR is the Gain Bandwidth Product. From what has been gathered from general information sources this is as the word describes a product of open loop gain and bandwidth and is constant for a specific op-amp. From these equations we have that limiting the

bandwidth to $0.5[Hz]$ or lower will require a unreasonably large capacitor. If aliasing is to be avoided we will most likely need as large a capacitor as can be reasonably installed and subsequent a digital low pas filter on sampled data will be needed. Currently the op-amp AD8617ARM from Analog Devices is installed with $C_F = 1[nF]$ and $R_F = 500[\Omega]$ giving a bandwidth requiring a very high sample rate to avoid aliasing and a setup not far from being unstable.

While AD8617ARM op-amp works and the current needed $50[uA]$ is very small compared to other instruments. A quick search give many alternatives to this op-amp using significantly less power while also being medical grade op-amps expected to be more reliable. One such example is OPA2379 from Texas Instruments using only $5.5[uA]$. Unfortunately there was not time available to properly find and test alternatives.

The Sun simulator runs at a step time of $1[s]$ and as tested here, at nadir pointing rotation rates a first order low pas filter with cut off frequency at $0.5[Hz]$ causes negligible error. And a faster sampling rate of the sensor followed by a digital filter should give even less. For these reason the op-amp has not been simulated in any other way than a amplification and conversion to volt by 500 times and a idealized 12-bit ADC quantizer simulink block. This gives us sampled voltage from 0 to 1 as discrete values from 0 to $2^{11} - 1$ and a vector of measured values ***SunSenMeas*** containing the elements $SunSenMeas_{pi}$

$$SunSenMeas_{pi} = I_{pi} \cdot 500 \cdot (2^{11} - 1) \quad (4.24)$$

4.3 Sun Vector Estimation

In this section 4 different estimation algorithms are suggested and as far as possible reasoned for and with results shown in plots. Simulation results will usually be given for all the algorithms and photodiode configurations illustrated in figures 3.7 to 3.13.

Before sampled Sun sensor measurements is used to estimate a Sun vector, they will likely need digital low pas filtering and down sampling as talked about in subsection 4.2.2. Noise is not implemented in the simulation. Only a conversion of the data back to irradiance as shown in the equation bellow.

$$E_{pi} = \frac{SunSenMeas_{pi}}{500 \cdot (2^{11} - 1)K_{Ri}} \quad (4.25)$$

(4.26)

Parameters used in all the simulations are given in table 4.3.

General Simulation Parameters	
Satellite	ESTCUBE 1, Sun synchronous day night orbit of average height 665[km]
Satellite Rotation Rate	1.9[deg/sec]
UTC Start Time	Day: 02, Month: 07, Year: 2016
Step Time	1 sec
Reflectivity Map	TOMS annual average of 2005
Photodiode	BPW34FS, $E_{\theta_0} = 188.1[W/m^2]$

4.3.1 Pseudoinverse

Using the fact that reflected light from Earth on average is around 30% of incident light from the Sun, and cosine of the FOV limits $FOV_{70} = \cos(70) = 0.34$ and $FOV_{75} = \cos(75) = 0.26$. It can be said that photodiodes with output above $E_{S\theta_0} \cdot FOV_{70}$ can usually see the Sun and measured values bellow are mostly only from Earth. These FOV limits are physical limits simulated as described in section 4.2.1. To estimate a Sun vector only E_{pi} values above $E_{\theta_0} \cdot FOV_{\theta}$ and corresponding photodiode normals are needed. This vector and matrix is expressed with \mathbf{E}_{ps} and H_s giving Sun vector estimation equation with the pseudoinverse expressed as shown bellow 4.27.

$$\tilde{\mathbf{s}}_b^b = (H_s^T H_s)^{-1} H_s^T \mathbf{E}_{ps} \quad (4.27)$$

With photodiode normals in H expressed in the body frame the estimated Sun vector is naturally also in the body frame pointing from the body frame $\tilde{\mathbf{s}}_b^b$. When a photodiode configuration with a FOV limit is simulated this limit is used to chose photodiodes in the estimates as described above. The first simulation is with the original configuration of photodiodes mounted flatly onto the sides of the satellite with full FOV as illustrated in figure 3.7. The estimation error can be seen in figure 4.6.

The simulation is over a period of 24 hours to illustrate how different parts of Earth affect the error. The largest Zenith error at the orbit of $2.5 \cdot 10^4 [sec]$ is caused by the satellite passing over a part of a pole with more ice or snow. The error peeks are not only caused by increased reflectivity but also the angle between Albedo vectors and the Sun vector decreasing as the satellite moves towards the poles. The large difference between The North and South Pole (start and end of a orbit) are likely there because one pole is tilted more towards the Sun. The largest error in zenith is at 25[deg] while the smallest is at around 18[deg]. Azimuth error is notably smaller and usually bellow 5[deg].

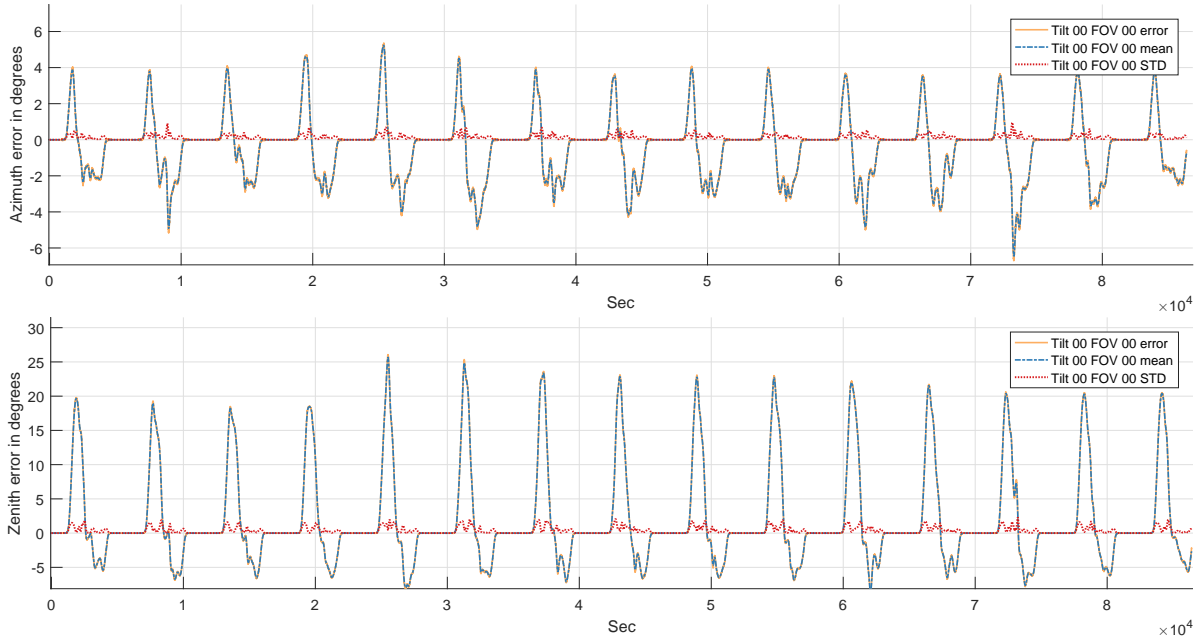


Figure 4.6: Pseudoinverse, equation 4.27 Sun vector estimate error in inertial frame with photo-diode configuration 0 3.7. Standard deviation and mean of the error are over a Hanning window of 181 samples

Admittedly this estimate is not necessarily the best estimate that can be done for this configuration. It is expected that some improvement can be made by using only photo diodes experiencing the most radiance instead of all the photodiodes. Next, simulation results are given and discussed for all the configurations 3.7 to 3.13 but only for the two orbits from $1.8 \cdot 10^4$ to $2.8 \cdot 10^4$ seconds. These two orbits were chosen as good examples of what is worst and best during the specific day simulated here and to better illustrate the estimation error.

From figure 4.7 we can see that there is a significant improvement in error to below 5 deg for major parts of an orbit with configurations using a FOV limit at an angle of 70 deg. When the irradiance from Earth onto a photodiode moves above $E_{S0_0} \cdot FOV_{70}$ the error increases drastically. This can be seen as a sharp increase in STD in the first orbit caused by sensors moving in and out of orientations where this limit is crossed. In the second orbit it can be seen as a sharper increase of mean error as several sensors stay in orientations over longer periods of time where this happens. The error surprisingly peaks above the estimate obtained with the original configuration. A plot of measured Albedo(after ADC), separated from Sun input, together with the

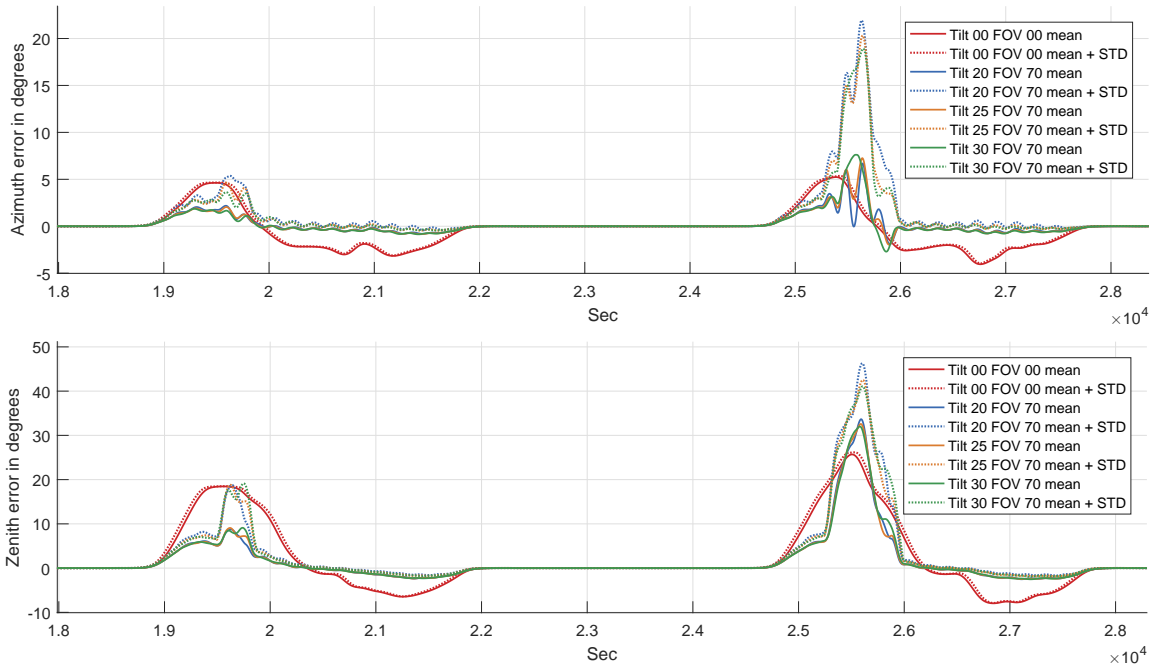


Figure 4.7: Pseudoinverse 4.27 Sun Vector estimate error in the inertial frame. A centered Hanning window of 181 samples has been used for the mean and standard deviation(STD).

FOV limit $E_{S\theta_0} \cdot FOV_{70}$ is shown in figure 4.8.

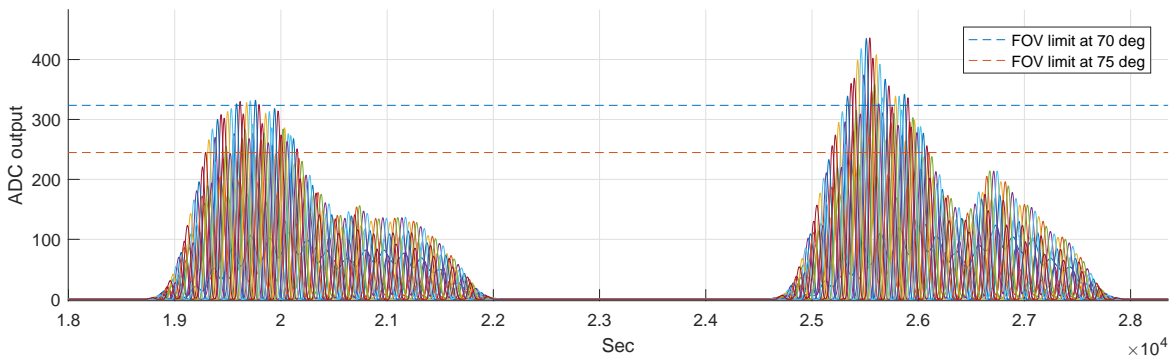


Figure 4.8: Plots without legend are here Measured Albedo on the 14 photo diodes of configuration 3.13 after ADC.

It can also be seen that a FOV limit of 75[deg] leads to a inclusion of more photodiodes sensing Earth reflected light. This leads to a major increase in estimation error as can be seen in figure 4.9. From figure 4.9 and 4.7 it can also be seen that different photodiode orientations barely affect the mean error and the STD value increases slightly with reduced photodiode tilt away from satellite panel normal.

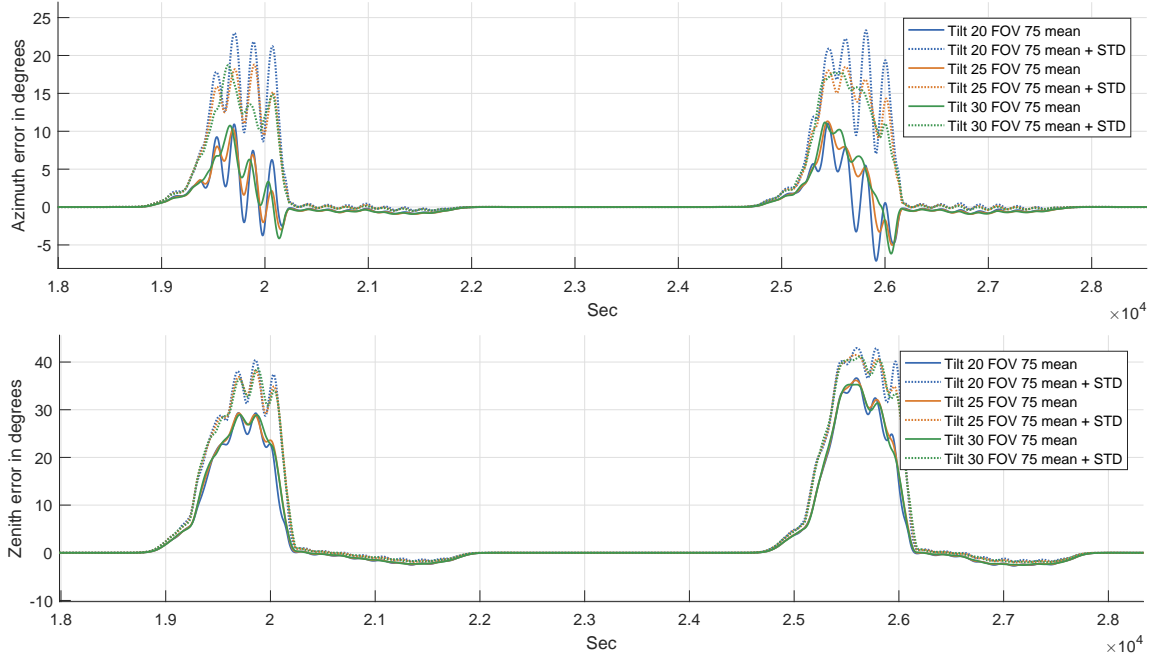


Figure 4.9: Pseudoinverse 4.27 Sun Vector estimate error in the inertial frame plotted in spherical coordinates. A centered Hanning window of 181 samples has been used.

4.3.2 Linear Least Squares Sun Vector Estimation

A linear least squares unconstrained solution that is optimal for a weighting matrix W can be used and expressed as follows.

$$\tilde{\mathbf{s}}_p^b = (H^T W H)^{-1} H^T W \mathbf{E}_p \quad (4.28)$$

The weighting matrix W can be a measurement covariance matrix R^{-1} . Under this condition the solution is optimal for zero-mean measurement error according to the Gauss Markov Theorem Crassidis and Junkins (2011). From Springmann (2013) we have that higher covariance values in R often is used to weight photodiodes with more incident light from Earth to improve estimates. How it is determined that a photodiode experiences more Earth reflected light is not mentioned. One can reason that photo diodes experiencing more incident light will be those

observing the Sun. Therefore E_{ps} is tested as diagonal weights in W . Photodiodes used in estimates are selected using the FOV limit as described previously for the pseudo inverse, resulting in the following equation 4.30

$$W_s = \text{diag}(E_{ps}) \quad (4.29)$$

$$\tilde{\mathbf{s}}_b^b = (H_s^T W_s H_s)^{-1} H_s^T W_s E_{ps} \quad (4.30)$$

The stated equations above are executed with inputs and outputs in the following matlabfunction.

$$[\tilde{\mathbf{s}}_b^b] = \text{LeastSqrSunVectorEsti}(FOV, H, E_p) \quad (4.31)$$

As done for previous simulations, mean and STD of the error between $\tilde{\mathbf{s}}_b^i$ and simulated Sun vector \mathbf{s}_b^i given to the sensors are plotted bellow using spherical coordinates in figures 4.10 and 4.11.

In this case there is also barely any difference in error between the different photodiode orientations, and the trend of increasing tilt giving slightly reduced STD is also present. The improvement gained compared to the pseudo inverse from using the least squares solution is most visible in zenith and azimuth error peaks of the second orbit. In zenith the peak mean error at $2.55 \cdot 10^4 [sec]$ is reduced by approximately 5[deg] in both the case of 70[deg] FOV 4.10 and 75[deg] FOV 4.11. The improvement in azimuth is around 2.5[deg] to 3[deg] in both cases. It can also be seen here that the least squares solution with a weighting matrix of the form used here does not have any effect on the original configuration of 0 tilt and full 90[deg] FOV. Finally this subsection is rounded off with a plot of raw error data together with mean and STD to illustrate the result in more detail 4.12.

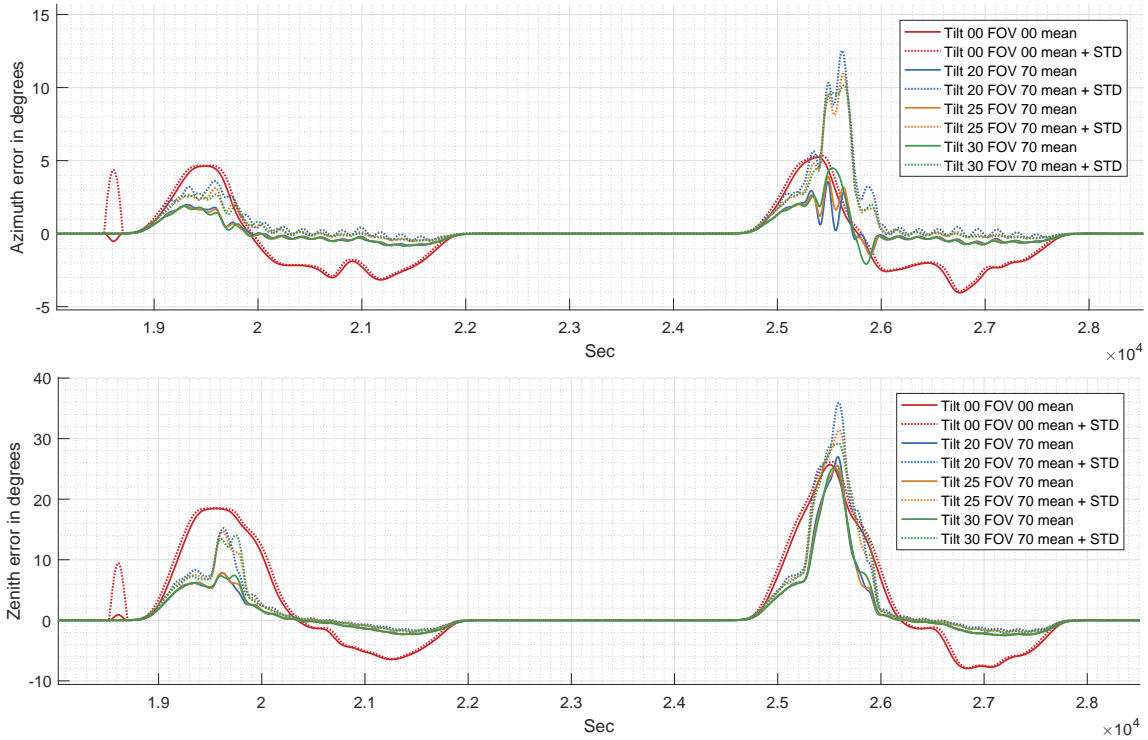


Figure 4.10: Least Squares 4.30 Sun Vector estimate error in the inertial frame. A centered Hanning window of 181 samples has been used.

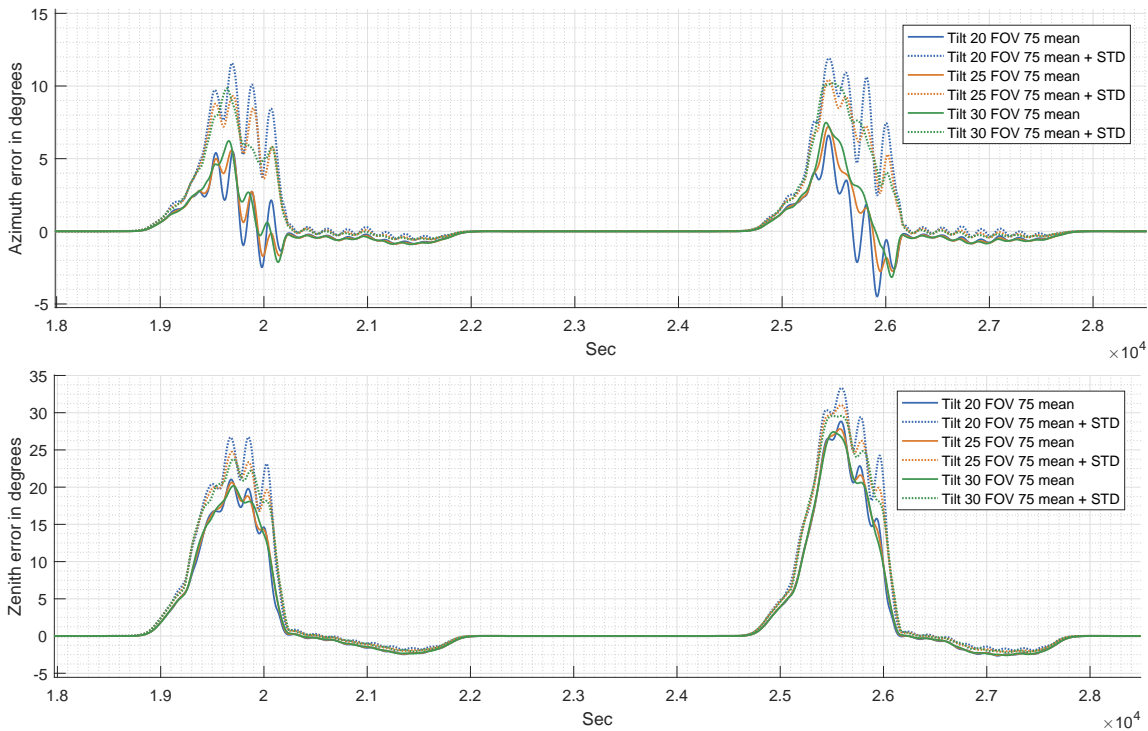


Figure 4.11: Least Squares 4.30 Sun Vector estimate error in the inertial frame. A centered Hanning window of 181 samples has been used.

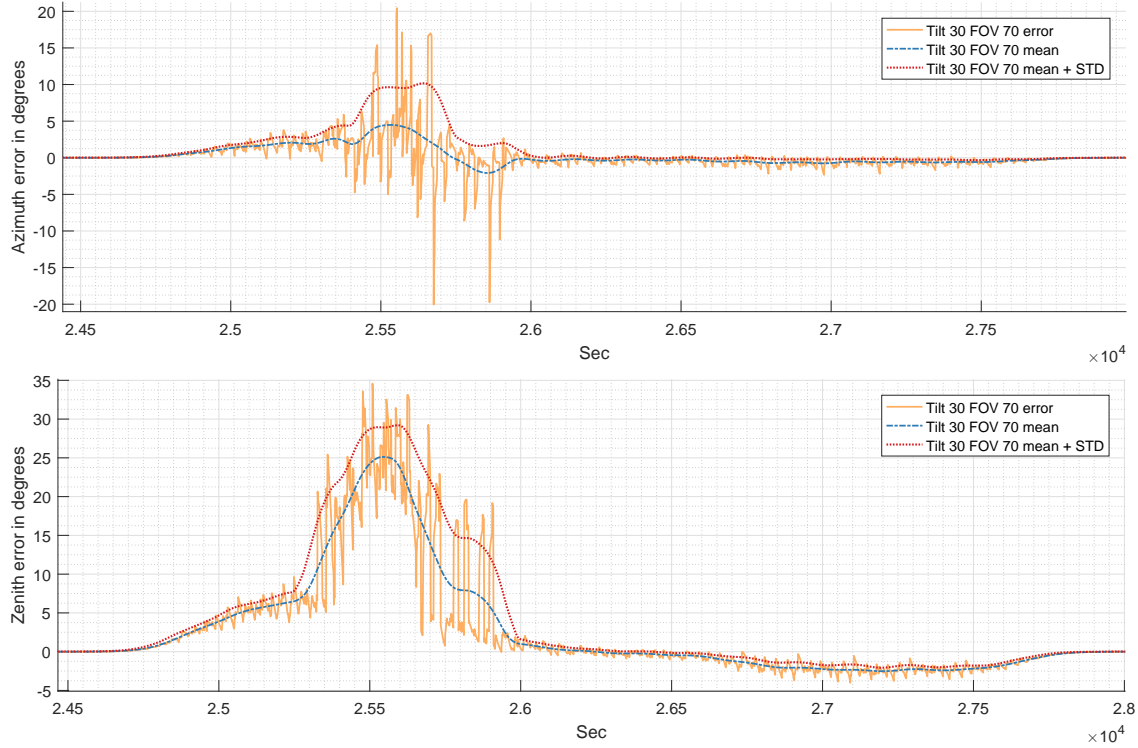


Figure 4.12: Least Squares 4.30 Sun Vector estimate error in the inertial frame. A centered Hanning window of 181 samples has been used.

4.3.3 Albedo-Sun Vector Estimate

So far the FOV limits have been used to choose photodiodes for a Sun vector. As an added bonus of the redundant photodiode configuration, a measured vector of light using three photodiodes should give the irradiance incident on the fourth photodiode. In all the configurations where photodiodes are tilted, at least 4 photodiodes should usually see a vector of irradiance if all of them are functional. Building on this idea the FOV limits can be used to first estimate a Albedo vector, that should often improve the final estimate.

First a estimate of a Earth reflected irradiance vector is made using photodiodes measuring irradiance bellow $E_{S\theta_0} \cos(FOV)$. E_{pa} and H_a is used as notation for measurements satisfying this condition and corresponding photodiode normal vectors.

A diagonal weighting matrix is not used in equation 4.32 because E_{pa} will also contain noise like

components as large as $E_{S\theta_0} \cos(FOV)$ from the Sun. This is caused by simulated FOV limiting leading to Sun input not instantly disappearing after the limit, but dropping off quickly to zero as described in subsection 4.2.1. This Sun input is below $E_{S\theta_0} \cos(FOV)$ and thus included in the estimate of $\tilde{\mathbf{a}}_b^b$ causing a noise like effect it is not desirable to increase with a weighting matrix.

$$\tilde{\mathbf{a}}_b^b = (H_a^T H_a)^{-1} H_a^T \mathbf{E}_{pa} \quad (4.32)$$

$$\tilde{\mathbf{E}}_{pa} = H \tilde{\mathbf{a}}_b^b \quad (4.33)$$

The estimated Albedo vector $\tilde{\mathbf{a}}_b^b$ is mapped back onto the photodiodes to find the effect not included in \mathbf{E}_{pa} . This gives a new estimate of measured Albedo irradiance $\tilde{\mathbf{E}}_{pa}$ that is actively constrained to values above zero.

$$\tilde{\mathbf{E}}_{ps} = \mathbf{E}_p - \tilde{\mathbf{E}}_{pa} \quad (4.34)$$

Here $\tilde{\mathbf{E}}_{ps}$ is a estimate of measured Sun irradiance. The notation \mathbf{E}_{ps} is reused to contain all values in $\tilde{\mathbf{E}}_{ps}$ larger or equal to $E_{S\theta_0} \cos(FOV)$ and H_s is a matrix containing corresponding photodiode normal vectors. The final estimated Sun vector is found with the equation below.

$$W_s = \text{diag}(\mathbf{E}_{ps}) \quad (4.35)$$

$$\tilde{\mathbf{s}}_b^b = (H_s^T W_s H_s)^{-1} H_s^T W_s \mathbf{E}_{ps} \quad (4.36)$$

The stated equations above are executed with inputs and outputs for the following matlabfunction.

$$[\tilde{\mathbf{E}}_{pa}, \tilde{\mathbf{E}}_{ps}, \tilde{\mathbf{s}}_b^i] = \text{AlbSunVectorEsti}(FOV, H, \mathbf{E}_p) \quad (4.37)$$

As done for previous simulations, mean and STD of the error between $\tilde{\mathbf{s}}_b^i$ and input Sun vector \mathbf{s}_b^i to the sensors are plotted below using spherical coordinates in figures 4.13 and 4.14

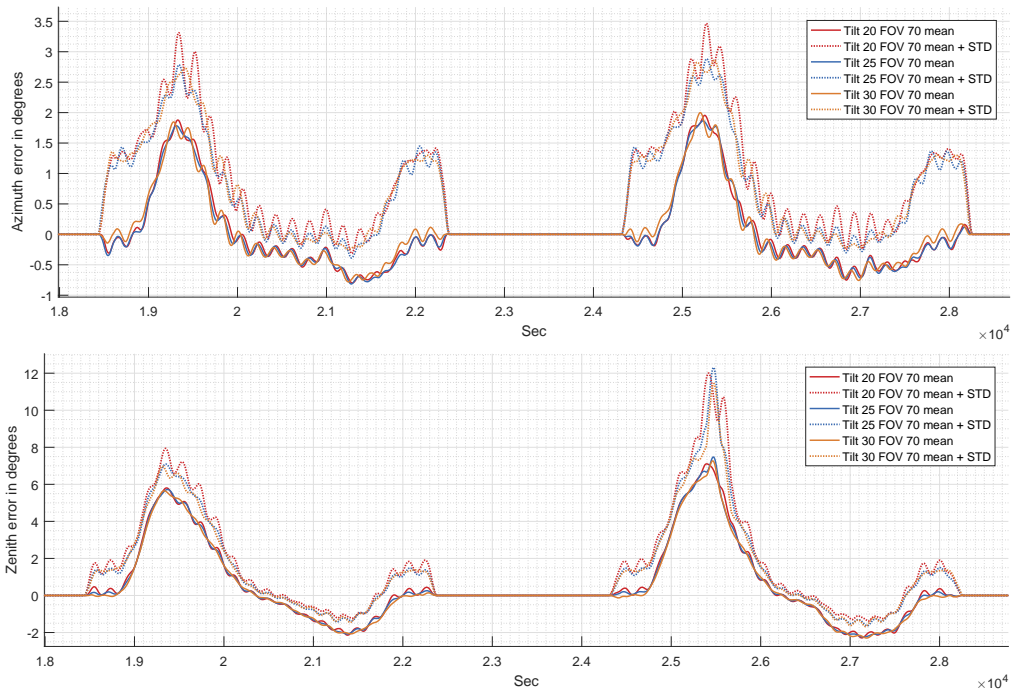


Figure 4.13: Sun vector estimation error is found in the inertial frame. A centered Hanning window of 181 samples has been used on the mean and STD plots. Sun estimate improved using a Albedo estimate. Equations used are 4.32 to 4.36.

The resulting mean Sun vector error given in figure 4.13 for a 70[deg] FOV limit has been improved to bellow 8[deg] in zenith on the second orbit. On the First orbit the mean zenith error is bellow 6[deg]. For the 75[deg] FOV limit, results illustrated in figure 4.14 gives a peak of mean Zenith error reduction to bellow 15[deg]. The Azimuth error for the 70[deg] FOV limit illustrated in figure 4.13 is mostly unchanged except for a significant reduction in error STD. Worth pointing out is also that the overall improvement in estimation error comes at the price of slightly

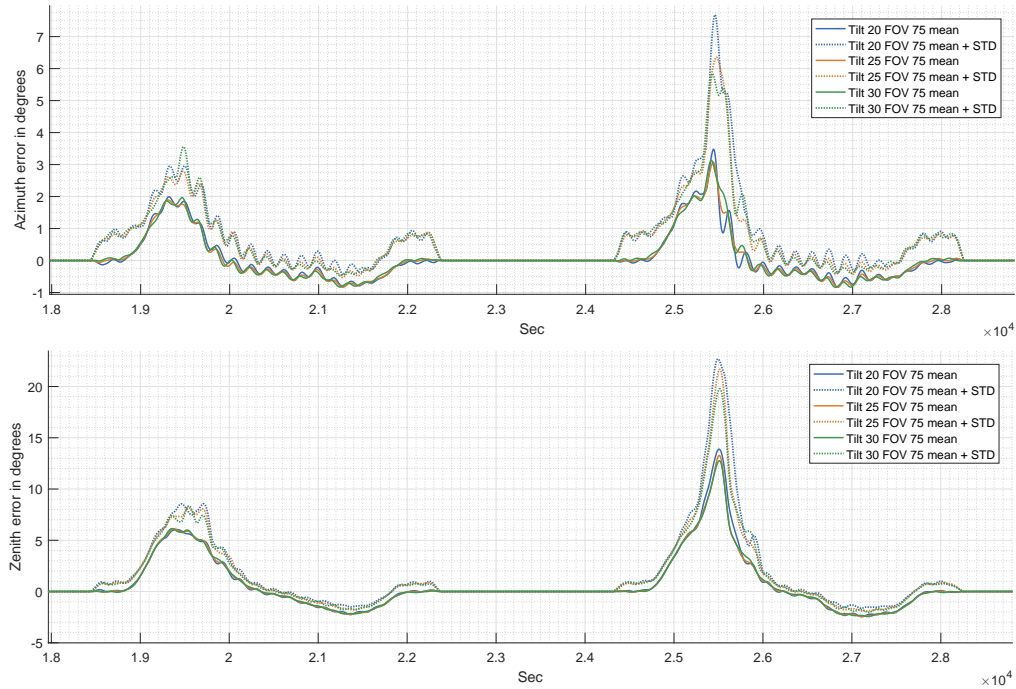


Figure 4.14: Sun estimate improved using an Albedo estimate. Equations used are 4.32 to 4.36. The estimation error is found in the inertial frame. A centered Hanning window of 181 samples has been used on the mean and STD calculation.

more noise at the start and end of an orbit when there is no incident albedo making the estimate unnecessarily noisy. This is as mentioned previously most likely caused by equation 4.32 also using slivers of incident Sun irradiance present only shortly after the FOV limit.

4.3.4 Sun-Albedo-Sun Vector Estimate

Knowing that the previous method to estimate the Albedo effect on the photo diodes gave good results. And that there are significant error sources in the data used to estimate the Albedo vector. A initial estimate of the Sun to find the Albedo vector and its effect on photodiodes should avoid the problems in the previous algorithm. The Albedo-Sun vector estimate could even be used to find the initial Sun Vector. For these reasons the following Sun vector estimation scheme is suggested.

The estimated Sun vector should have the known length $E_{S\theta_0}$, this can be used to correct the initial estimate $\tilde{\mathbf{s}}_b^b$

$$\hat{\mathbf{s}}_b^b = E_{S\theta_0} \frac{\tilde{\mathbf{s}}_b^b}{\|\tilde{\mathbf{s}}_b^b\|} \quad (4.38)$$

$$\tilde{\mathbf{E}}_{ps} = H\hat{\mathbf{s}}_b^b \quad (4.39)$$

Naturally as done in the previous subsections $\tilde{\mathbf{E}}_{ps}$ and $\tilde{\mathbf{E}}_{pa}$ is limited to values above zero. From $\tilde{\mathbf{E}}_{pa}$ only these values are taken and used in \mathbf{E}_{pa} and corresponding photodiode normal vectors are in the matrix H_a .

$$\tilde{\mathbf{E}}_{pa} = \mathbf{E}_p - \tilde{\mathbf{E}}_{ps} \quad (4.40)$$

$$\mathbf{W}_a = \text{diag}(\mathbf{E}_{pa}) \quad (4.41)$$

$$\tilde{\mathbf{E}}_{pa} = H((H_a^T \mathbf{W}_a H_a)^{-1} H_a^T \mathbf{W}_a \mathbf{E}_{pa}) \quad (4.42)$$

Using the new estimate $\tilde{\mathbf{E}}_{pa}$ and measured irradiance values \mathbf{E}_p , $\tilde{\mathbf{E}}_{ps}$ is found. Only values in $\tilde{\mathbf{E}}_{ps}$ above $E_{S\theta_0} \cos(FOV)$ is used in \mathbf{E}_{ps} and H_s contain the corresponding photodiode normal vectors. Using this the final Sun vector estimate is found as illustrated in the equations bellow.

$$\tilde{\mathbf{E}}_{ps} = \mathbf{E}_p - \tilde{\mathbf{E}}_{pa} \quad (4.43)$$

$$W_s = \text{diag}(\mathbf{E}_{ps}) \quad (4.44)$$

$$\tilde{\mathbf{s}}_b^b = (H_s^T W_s H_s)^{-1} H_s^T W_s \mathbf{E}_{ps} \quad (4.45)$$

The stated equations are executed with inputs and outputs as given bellow for the following matlabfunction

$$[\tilde{\mathbf{E}}_{pa}, \tilde{\mathbf{E}}_{ps}, \tilde{\mathbf{s}}_b^b] = \text{SunAlbSunVectorEsti}(\tilde{\mathbf{s}}_b^b, FOV, H, \mathbf{E}_p) \quad (4.46)$$

The first simulation presented here uses the initial estimate of $\tilde{\mathbf{s}}_b^b$ found with the linear least squares estimate $\text{LeastSqrSunVectorEsti}(FOV, H, \mathbf{E}_p)$. The simulation results are given bellow in figures 4.15

It was decided that it was sufficient to only present results on the 70[deg] FOV case because there was nothing new worth mentioning in other simulation results. Shortly described, estimates with 75[deg] FOV gave worse results when the reflected light from Earth moved above $E_{S\theta_0} \cos(75)$. In Figure 4.15 it is first clear that this method generates significantly less high frequency error compared to the previous method, when there is less Albedo incident on the satellite. The mean Zenith error in the first orbit is actually bellow 5[deg] in the case of 25[deg] and 30[deg] tilt, slightly better than the Albedo-Sun estimate. There is also a observable difference between these cases and the 20[deg] tilt case in both orbits. But in the second orbit

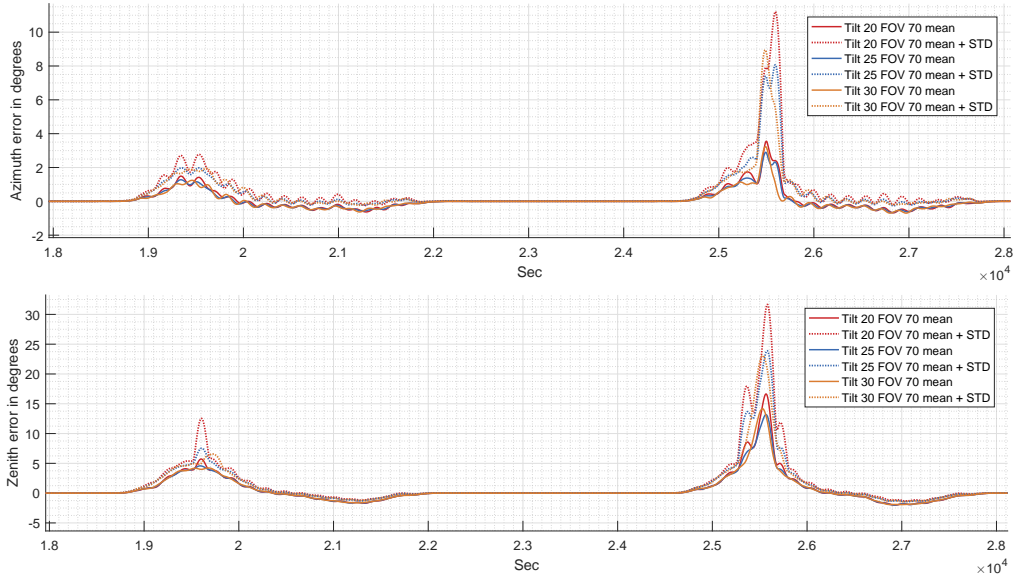


Figure 4.15: Sun-Albedo-Sun estimate results presented in terms of error. The estimation error is found in the inertial frame. A centered Hanning window of 181 samples has been used on the mean and STD calculation.

,Sun-Albedo-Sun estimate mean error peak is worse than the Albedo-Sun result and better than the Least Squares estimate with a peak error around 15[deg]. The Azimuth error follows the same trend also present in the zenith error.

The second simulation presented here finds the initial estimate of \tilde{s}_b^b using the Albedo-Sun estimation method $\text{AlbSunVectorEsti}(FOV, H, E_p)$, but with $\text{diag}(E_a)^{-1}$ as weighting matrix for the albedo estimate instead of the pseudo inverse. This was done to reduce the generated high frequency error in the initial estimate, the result of this is shown in figure 4.16. The simulation results for the Sun-Albedo-Sun method is given in figure 4.17. Only the case of 20[deg] tilt is given because the difference between configurations has already been demonstrated to be relatively small.

The final Sun vector estimation error shown in figure 4.17 is better than the results demonstrated with any of the previous methods. In zenith the mean error peak of the first orbit is now bellow 5[deg] and bellow 6.25[deg] in the second orbit. The Azimuth error is clearly greatly improved in the second orbit while it is difficult to read any difference on the first orbit.

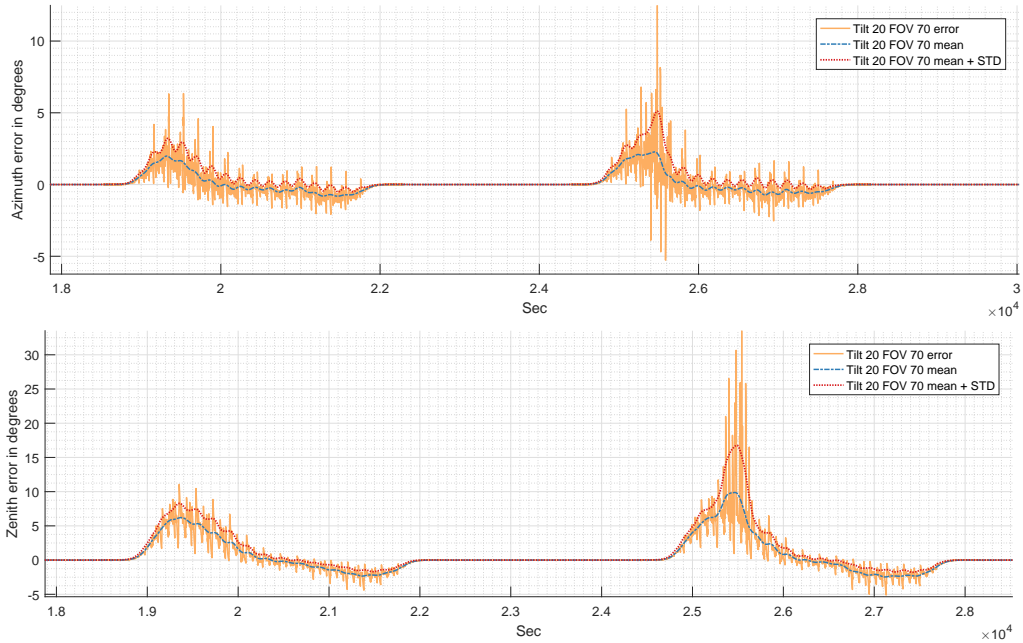


Figure 4.16: Albedo-Sun estimate results presented in terms of error in spherical coordinates. The estimation error is found in the inertial frame. A centered Hanning window of 181 samples has been used on the mean and STD calculation. $diag(E_a)^{-1}$ is used as weighting matrix instead of $diag(E_a)$

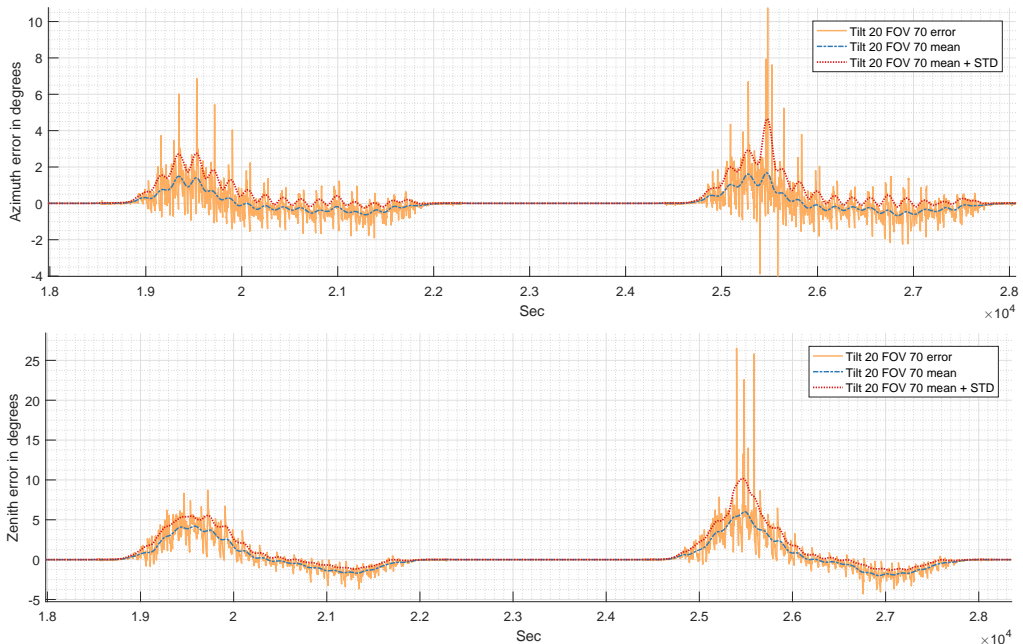


Figure 4.17: Sun-Albedo-Sun estimate results presented in terms of error. The estimation error is found in the inertial frame. A centered Hanning window of 181 samples has been used on the mean and STD calculation. The Alb-Sun estimation result in figure 4.16 is used as input for the Sun-Albedo-Sun estimate presented here.

Chapter 5

Summary, Conclusion and Further Work

In the section of summary and conclusions results are first presented on the work of finding a gyroscope for the NUTS cube sat project. Before simulation results and conclusions are given for Sun vector estimation and Sun sensor output. The same order is also followed in the discussion and recommendation for further work.

5.1 Summary and Conclusion

Finding a gyroscope that can be easily determined as better in all aspects compared to competing alternatives is not possible simply using data sheets. A good overview of what is available on the market is given and three alternatives are recommended for practical testing to find out which one is best suited to make pointing of the satellite work. A good comprehensive description of gyroscope errors has been laid out in the back ground material. Three different methods of compensating for temperature varying bias on MEMS gyroscopes has been found in literature. The most commonly used is a forth order polynomial in temperature. And there may also

be a additional thermal effect dynamically induced by acceleration/gravity that should be kept in mind when a gyroscope is tested. A third method involves mounting equal gyroscopes with sensing axes in opposing directions and using the measurements to cancel out the zero rate temperature induced bias. It is also found in literature that many MEMS gyroscopes may have errors such as the scale factor and bias changing from power on, to power on.

A complete simulation of a tumbling satellite with incident light from both the Sun and Earth is implemented. This work was largely based on previous work by [Pigned \(2015\)](#) on the prediction algorithms for the NUTS CubeSat and [Bhanderi and Bak \(2005\)](#) giving the Earth albedo model. Two photodiodes are found and argued for as good alternatives for a pyramid Sun sensor. A issue related to degradation of sensitivty have been found in two cited articles and a tested solution is given in one of them. Six different configurations of such a sensor is suggested with physically limited FOV and simulated with four different methods of Sun vector estimation. It is shown that straight forward use of the pseudo inverse without choosing photodiodes can give estimation error as large as $25[deg]$. It is also shown that this error can be improved to bellow $5[deg]$ for large parts of illuminated orbit by using a physical FOV limit to chose photodiodes used in a Sun vector estimate. Further more two methods of Sun vector estimation that this author has not seen anywhere else in literature before is presented. Both methods used a estimate of a Earth reflected light vector to improve the mean error peaks of the estimated Sun vector. The first method pushes the mean error bellow $8[deg]$ where the error was as high as $25[deg]$ with a pseudo inverse or a least squares estimate. The second method pushes the mean error further down to bellow $6.5[deg]$. Finally based on these simulations, physically limiting the FOV of photodiodes at $70[deg]$ away from photodiode normals gives clear advantages for a pyramid Sun sensor on a tumbling satellite. It is also shown that measurements from a redundant configuration of photodioes that can see the entirety of the attitude sphere contains sufficient information to not only estimate a Sun vector but also a Albedo.

5.2 Discussion

On the subject of trying to choose a gyroscope for an attitude estimation and control situation. It was surprising to find out that MEMS gyroscope errors can be as unpredictable as presented in the background material suggests. This became a huge problem in the original plan for answering this task and a huge lesson learned. When work on this task started it was assumed that datasheets were sufficient for choosing an appropriate gyroscope. But they are clearly lacking because they never give any information on repeatability of the error characteristics. It was also difficult to find detailed sources on MEMS gyroscope error characteristics. As a result much more time was spent on researching literature to learn about gyroscope errors than was expected.

The largest Sun vector estimation error comes from the poles and is largest when they are most tilted towards the Sun. It has not been investigated exactly when in summer the largest error can be expected but the start of July should not be far away from that. The annual average of Earth reflection data should make the simulation results shown worse than a summer average. Based on this the Sun vector estimate errors shown here should be a good example of the worst case during summer. Simulations were also done for days in winter, autumn, and spring with the annual average reflection map. Unfortunately those results are not documented here but it was observed that the winter period gave larger mean error peaks while autumn and spring unsurprisingly gave smaller than both summer and winter. With the reflection map being an annual average, variations due to clouds are naturally not present. It is stated in the Matlab® albedo toolbox [Bhanderi \(2008\)](#) tech notes that the difference in simulated current output from sensors with a daily albedo map versus the annual average is very small to degree where mean data can typically be applied. An issue that cannot be immediately laid to rest is that in section [2.3.3](#) it is shown that Earth reflectivity is much higher over Oceans in the UV spectrum than it is in the spectral ranges where suggested photodiodes measure light. And the UV spectrum is what the reflectivity map used here is for. Fortunately having a simulation that may have more difficult conditions than real life is not a bad thing when the simulations are used for design of a real

life application because it leaves head room for mistakes. It may also be possible to find a more appropriate reflection map from another source.

A clear weakness to this work are the unexplored methods of choosing the best photodiodes for Sun vector estimates with the original configuration 3.7. For example finding the photodiode with most incident light and choosing two other photodiodes with overlapping FOV, normal vectors linearly independent and with most or least incident light should give a more fair estimate for comparison. It can therefore not be concluded here that suggested photodiode configuration and estimation methods are definitely better than what may be achievable with the original configuration. But with this work the tools are available for someone else to do further testing with Sun vector estimation algorithms. Another weakness with the results shown here is that they are only for one randomly chosen rotation rate higher than the nadir pointing case. The high frequency error present is very likely to a degree a result of this. For a slower tumbling rate it is not difficult to imagine that the Sun vector error may for longer periods be closer to $mean \pm STD$. In other words a mean error value could on occasion be higher or lower in a case of slower tumbling. The actual result of this in an attitude estimate should be investigated.

5.3 Further Work

On the Sun sensor the next step would be to verify the equations of section 3.2 for photodiode current output. This should be achievable by using SMARTS2 Gueymard (1995) to generate irradiance spectra hitting a surface at the location and time a measurement of current from the relevant photodiode is performed. While simulations of the measured Sun vector have been performed here we have not used it to find an estimate of orientation. This being the value of importance it may be that the original configuration and proper selection of photodiodes as discussed above for Sun vector estimation may give sufficient attitude estimates. Therefore relevant attitude estimation algorithms should be tested together with this simulation before the final Sun sensor solution is decided upon. Such a simulation should also include a proper model

of a gyroscope and magnetometer with errors to conclude how good a gyroscope is needed to get a estimated rotation rate that attitude control can work with.

Bibliography

Hamamatsu. URL:<http://www.hamamatsu.com/us/en/index.html>. Accessed: 2016-06-29.

Optical Filter Shop. URL: <http://opticalfiltershop.com>. Accessed: 2016-06-29.

Photodiode characteristics and application. URL: <http://www.osioptoelectronics.com/application-notes/AN-PhotodiodeParameters-Characteristics.pdf>. Accessed: 2016-06-29.

Position Sensitive Diode Characteristics. URL: [http://www.osioptoelectronics.com/application-notes/AN-Position-Sensing-Photodiodes\(PSDs\).pdf](http://www.osioptoelectronics.com/application-notes/AN-Position-Sensing-Photodiodes(PSDs).pdf). Accessed: 2016-06-29.

Solar-MEMS. URL: <http://www.solar-mems.com/en/products/renewable-energy>. Accessed: 2016-06-29.

(2014). Ieee standard for sensor performance parameter definitions. *IEEE Std 2700-2014*, pages 1–69.

Aggarwal, P. (2010). *MEMS-based integrated navigation*. Artech House.

Bhanderi, D. D. (2008). Earth Albedo Toolbox. URL: <http://www.mathworks.com/matlabcentral/fileexchange/11211-earth-albedo-toolbox>[cited 29 Jun 2016].

Bhanderi, D. D. and Bak, T. (2005). Modeling earth albedo for satellites in earth orbit. *AIAA Guidance, Navigation, and Control Proceedings*.

Burle, E. (2000). *Electro-optics handbook*. McGraw-Hill, New York.

Crassidis, J. L. and Junkins, J. L. (2011). *Optimal estimation of dynamic systems*. CRC press.

- Cutler, J., Springmann, J., Spangelo, S., and Bahcivan, H. (2011). Initial flight assessment of the radio aurora explorer.
- Czernik, S. (2004). Design of the thermal control system for compass-1. *University of Applied Sciences Aachen Germany*.
- El-Sheimy, N., Hou, H., and Niu, X. (2008). Analysis and modeling of inertial sensors using allan variance. *IEEE Transactions on instrumentation and measurement*, 57(1):140–149.
- Fossen, T. I. (2011). *Handbook of marine craft hydrodynamics and motion control*. John Wiley & Sons.
- Gerhardt, D., Palo, S., Li, X., Blum, L., Schiller, Q., and Kohnert, R. (2013). The colorado student space weather experiment (csswe) on-orbit performance.
- Gorski, K. M., Hivon, E., Banday, A., Wandelt, B. D., Hansen, F. K., Reinecke, M., and Bartelmann, M. (2005). Healpix: a framework for high-resolution discretization and fast analysis of data distributed on the sphere. *The Astrophysical Journal*, 622(2):759.
- Gottwald, M. and Bovensmann, H. (2010). *SCIAMACHY-Exploring the changing Earth's Atmosphere*. Springer Science & Business Media.
- Grewal, M. and Andrews, A. (2010). How good is your gyro [ask the experts]. *IEEE Control Systems*, 30(1):12–86.
- Gueymard, C. (1995). *SMARTS2: a simple model of the atmospheric radiative transfer of sunshine: algorithms and performance assessment*. Florida Solar Energy Center Cocoa, FL.
- Gueymard, C. A. (2001). Parameterized transmittance model for direct beam and circumsolar spectral irradiance. *Solar Energy*, 71(5):325–346.
- Jiancheng, F. and Jianli, L. (2009). Integrated model and compensation of thermal errors of silicon microelectromechanical gyroscope. *IEEE Transactions on Instrumentation and Measurement*, 58(9):2923–2930.
- Kelso, T. (2015). Celestrak. *Public Domain Satellite Tracking Data*, URL: <http://celestrak.com/>[cited 29 Jun 2016].

- Martin, H., Groves, P., Newman, M., and Faragher, R. (2013). A new approach to better low-cost mems imu performance using sensor arrays.
- Nassar, S. (2005). *Improving the inertial navigation system (INS) error model for INS and INS/DGPS applications*. National Library of Canada= Bibliothèque nationale du Canada.
- Niu, X., Li, Y., Zhang, H., Wang, Q., and Ban, Y. (2013). Fast thermal calibration of low-grade inertial sensors and inertial measurement units. *Sensors*, 13(9):12192–12217.
- Ortega, P., López-Rodríguez, G., Ricart, J., Domínguez, M., Castañer, L. M., Quero, J. M., Tarrida, C. L., García, J., Reina, M., Gras, A., et al. (2010). A miniaturized two axis sun sensor for attitude control of nano-satellites. *IEEE Sensors Journal*, 10(10):1623–1632.
- Park, B. S., Han, K., Lee, S., and Yu, M. (2015). Analysis of compensation for a g-sensitivity scale-factor error for a mems vibratory gyroscope. *Journal of Micromechanics and Microengineering*, 25(11):115006.
- Paulescu, M., Paulescu, E., Gravila, P., and Badescu, V. (2012). *Weather modeling and forecasting of PV systems operation*. Springer Science & Business Media.
- Perez, T., Smogeli, Ø. N., Fossen, T. I., and Sørensen, A. J. (2006). An overview of the marine systems simulator (mss): A simulink® toolbox for marine control systems. *Modeling, identification and Control*, 27(4):259–275.
- Pigned, A. (2015). Prediction Algorithms for the NUTS Attitude Estimator and Robust Spacecraft Attitude Stabilization using Magnetorquers . Master's thesis, Norwegian University of Science and Technology, Norway.
- Rohatgi, A. (2011). Webplotdigitizer. URL <http://arohatgi.info/WebPlotDigitizer/app>.
- Ryer, A. (1998). *Light Measurement Handbook*. International Light Inc.
- Scholz, A., Ley, W., Dachwald, B., Miao, J., and Juang, J. (2010). Flight results of the compass-1 picosatellite mission. *Acta Astronautica*, 67(9):1289–1298.

- Shafer, I., Powell, C., Stanton, J., and Grieneisen, D. (2008). Cubesat solar sensor final report. *Olin-NASA Research Group*, [online], <http://ece.olin.edu/nasa/projects/2008/sos/files/SOSReport.pdf> (Accessed 12 April 2011).
- Springmann, J. C. (2013). *Satellite attitude determination with low-cost sensors*. PhD thesis, University of Michigan.
- Springmann, J. C. and Cutler, J. W. (2014). On-orbit calibration of photodiodes for attitude determination. *Journal of Guidance, Control, and Dynamics*, 37(6):1808–1823.
- Stockwell, W. (2003). Angle random walk. *Application Note. Crossbow Technologies Inc*, pages 1–4.
- Titterton, D. and Weston, J. L. (2004). *Strapdown inertial navigation technology*, volume 17. IET.
- Weinberg, H. (2011). Gyro mechanical performance: The most important parameter. *Technical Article MS-2158. Analog Devices, Inc*, pages 1–5.
- Westgård, M. F. (2015). Software Design and Controller Evaluation for the ADCS on the NTNU Test Satellite. Master's thesis, Norwegian University of Science and Technology, Norway.
- Woodman, O. J. (2007). An introduction to inertial navigation. *University of Cambridge, Computer Laboratory, Tech. Rep. UCAMCL-TR-696*, 14:15.
- Yuksel, Y., El-Sheimy, N., and Noureldin, A. (2010). Error modeling and characterization of environmental effects for low cost inertial mems units. In *Position Location and Navigation Symposium (PLANS), 2010 IEEE/ION*, pages 598–612. IEEE.
- Øyvind Rein (2014). Developing an adcs prototype for ntnu test satellite. Master's thesis, Norwegian University of Science and Technology, Norway.